

KAgoshima Galactic Object survey with Nobeyama 45-metre telescope by Mapping in Ammonia lines (KAGONMA): Discovery of parsec-scale CO depletion in the Canis Major star-forming region

Yushi HIRATA,^{1*} Takeru MURASE,^{1,2} Junya NISHI,¹ Yoshito SHIMAJIRI,^{1,3,4,5}
Toshihiro OMODAKA,^{1,6} Makoto NAKANO,⁷ Kazuyoshi SUNADA,⁸ Takumi
ITO,^{1,9} and Toshihiro HANDA^{1,6*}

¹Department of Physics and Astronomy, Graduate School of Science and Engineering,
Kagoshima University, 1-21-35 Korimoto, Kagoshima, Kagoshima 890-0065, Japan

²Faculty of Engineering, Gifu University, 1-1 Yanagido, Gifu 501-1193, Japan

³National Astronomical Observatory of Japan, Osawa 2-21-1, Mitaka, Tokyo 181-8588, Japan

⁴Laboratoire d'Astrophysique (AIM), CEA/DRF, CNRS, Université Paris-Saclay, Université
Paris Diderot, Sorbonne Paris Cité, 91191 Gif-sur-Yvette, France

⁵Kyushu Kyoritsu University, Jiyugaoka 1-8, Yahatanishi-ku, Kitakyushu, Fukuoka, 807-8585,
Japan

⁶Amanogawa Galaxy Astronomy Research Center, Kagoshima University, 1-21-35 Korimoto,
Kagoshima, Kagoshima 890-0065, Japan

⁷Faculty of Science and Technology, Oita University, Oita 870-1192, Japan

⁸Mizusawa VLBI observatory, NAOJ 2-12, Hoshigaoka, Mizusawa, Oshu, Iwate 023-0861,
Japan

⁹Graduate School of Science and Technology, Kumamoto University, Kumamoto, 860-8555,
Japan

*E-mail: yushi.hirata.astro@gmail.com, k3233287@kadai.jp, handa@sci.kagoshima-u.ac.jp

Received 2023 August 15; Accepted 2023 November 7

Abstract

In observational studies of infrared dark clouds, the number of detections of CO freeze-out onto dust grains (CO depletion) at pc-scale is extremely limited, and the conditions for its occurrence are, therefore, still unknown. We report a new object where pc-scale CO depletion is expected. As a part of Kagoshima Galactic Object survey with Nobeyama 45-m telescope by Mapping in Ammonia lines (KAGONMA), we have made mapping observations of NH₃ inversion transition lines towards the star-forming region associated with the CMa OB1 including IRAS 07077–1026, IRAS 07081–1028, and PGCC G224.28–0.82. By comparing the spatial distributions of the NH₃ (1,1) and C¹⁸O ($J=1-0$), an intensity anti-correlation was found in IRAS 07077–1026 and IRAS 07081–1028 on the ~ 1 pc scale. Furthermore, we obtained a lower abundance of C¹⁸O at least in IRAS 07077–1026 than in the other parts of the star-forming region. After examining high density gas dissipation, photodissociation, and CO depletion, we concluded that the intensity anti-correlation in IRAS 07077–1026 is due to CO depletion. On the other hand, in the vicinity of the centre of PGCC G224.28–0.82, the emission line intensities of both

the NH_3 (1,1) and C^{18}O ($J=1-0$) were strongly detected, although the gas temperature and density were similar to IRAS 07077–1026. This indicates that there are situations where C^{18}O ($J=1-0$) cannot trace dense gas on the pc scale and implies that the conditional differences that C^{18}O ($J=1-0$) can and cannot trace dense gas are unclear.

Key words: ISM: abundances — ISM: clouds — ISM: molecules — radio lines: ISM — stars: formation

1 Introduction

Star formation is known to occur in cold, dense molecular clouds. In general, molecular clouds have a temperature of ~ 10 K, a volume density of about $10^2 - 10^5 \text{ cm}^{-3}$ (e.g., Dame et al. 2001; Bergin & Tafalla 2007), and are mostly composed of molecular hydrogen. The basic approach to measuring the mass of molecular clouds is to count the number of hydrogen molecules along the line-of-sight, called the H_2 column density, $N(\text{H}_2)$. However, radiation from molecular hydrogen, which is most abundant in molecular clouds, can only be detected from gas with a temperature above 80 K (Togi & Smith 2016). This means that it is not possible to observe H_2 emission from low-temperature regions directly related to the star-forming activity. Therefore, it is often used to determine the column density of CO molecules, $N(\text{CO})$, from the emission of CO isotopologues (e.g., ^{12}CO , ^{13}CO , and C^{18}O), which are the most abundant molecules after H_2 , and use the $[\text{CO}]/[\text{H}_2]$ abundance ratio to measure $N(\text{H}_2)$ indirectly.

$N(\text{CO})$ and $N(\text{H}_2)$ are not necessarily linear relationships (e.g., Frerking et al. 1982; Pineda et al. 2008; Ripple et al. 2013; Wang et al. 2019). In the relatively low temperature ($T < 20$ K) and high volume density ($n(\text{H}_2) > 10^4 \text{ cm}^{-3}$) regions, CO molecules freeze out and adsorb onto dust grains has been reported (e.g., Willacy et al. 1998; Tafalla et al. 2002). In the case of CO freeze-out onto dust grains, low- J lines of rare CO isotopologues such as C^{18}O or C^{17}O cannot trace the dense and cold gas (e.g., Caselli et al. 1999). This phenomenon, which is called CO freeze-out onto dust grains or depletion (hereafter CO depletion), is important for understanding the chemistry of molecular clouds because it not only affects the gas-phase chemistry but also promotes the surface reaction in dust grains.

CO depletion has been actively studied in nearby low-mass star-forming regions (e.g., Willacy et al. 1998; Caselli et al. 1999; Kramer et al. 1999; Bergin & Tafalla 2007). They have reported that CO depletion is frequently detected in starless cores at $T < 20$ K and $n(\text{H}_2) > 3 \times 10^4 \text{ cm}^{-3}$, and the spatial scale is mostly comparable to the size of the molecular cloud core (~ 0.05 pc). This is because the free fall timescale and the depletion timescale

coincide at the typical density of molecular cloud cores ($\sim 10^4 \text{ cm}^{-3}$).

In recent years, a small number of sources with pc-scale CO depletion have been reported from mapping observations of the CO isotopologue lines (Hernandez et al. 2011; Jiménez-Serra et al. 2014; Feng et al. 2016a, 2020; Gong et al. 2018; Sabatini et al. 2019, 2022; Lewis et al. 2021). In infrared dark clouds (IRDCs), which have higher densities than low-mass star-forming regions, pc-scale CO depletion is expected to be a common event; pc-scale CO depletion has been reported over a wide mass range, from low-mass IRDC, the Serpens filament ($20 - 66 M_\odot$, Roccatagliata et al. 2015; Gong et al. 2018) to IRDCs that massive enough to form high-mass stars (e.g., Sabatini et al. 2019; Feng et al. 2020). In low-mass star-forming regions, CO depletion occurs in cloud cores, whereas in IRDCs CO depletion occurs not only in cloud cores but also in clumps and filaments. However, previous studies are biased towards high-mass IRDCs that fulfil an empirical threshold for high-mass star formation, $M(r) > 870 M_\odot$ (radius/pc)^{1,33} (Kauffmann & Pillai 2010). To better understand pc-scale CO depletion, more low-mass/intermediate-mass sources with pc-scale CO depletion are required.

We focus on NH_3 molecular species. This molecule species is a good gas tracer in dense and cold regions, where star formation can occur (e.g., Myers & Benson 1983). The critical density of the NH_3 inversion transition lines are $\sim 2.0 \times 10^3 \text{ cm}^{-3}$ (Shirley 2015), which is comparable to that of the C^{18}O ($J=1-0$) lines ($\sim 2.0 \times 10^3 \text{ cm}^{-3}$, Pety et al. 2017). These molecule lines are a good combination for comparing the properties of gases other than density differences. Previous studies of NH_3 lines reported that NH_3 is a depletion-resistant species and does not freeze out only in cold and dense gas regions ($T < 20$ K, $n \geq 10^5 \text{ cm}^{-3}$), where carbon-bearing molecules have already been frozen out onto dust grains (e.g., Tafalla et al. 2002; Crapsi et al. 2007; Sipilä et al. 2019). Comparing the spatial distributions of NH_3 and C^{18}O may be able to detect pc-scale CO depletion. If this comparison can detect pc-scale CO depletion, it would be possible to separate the line-of-sight components, which is difficult to do with dust emission comparisons.

We observed NH_3 lines towards a star-forming re-

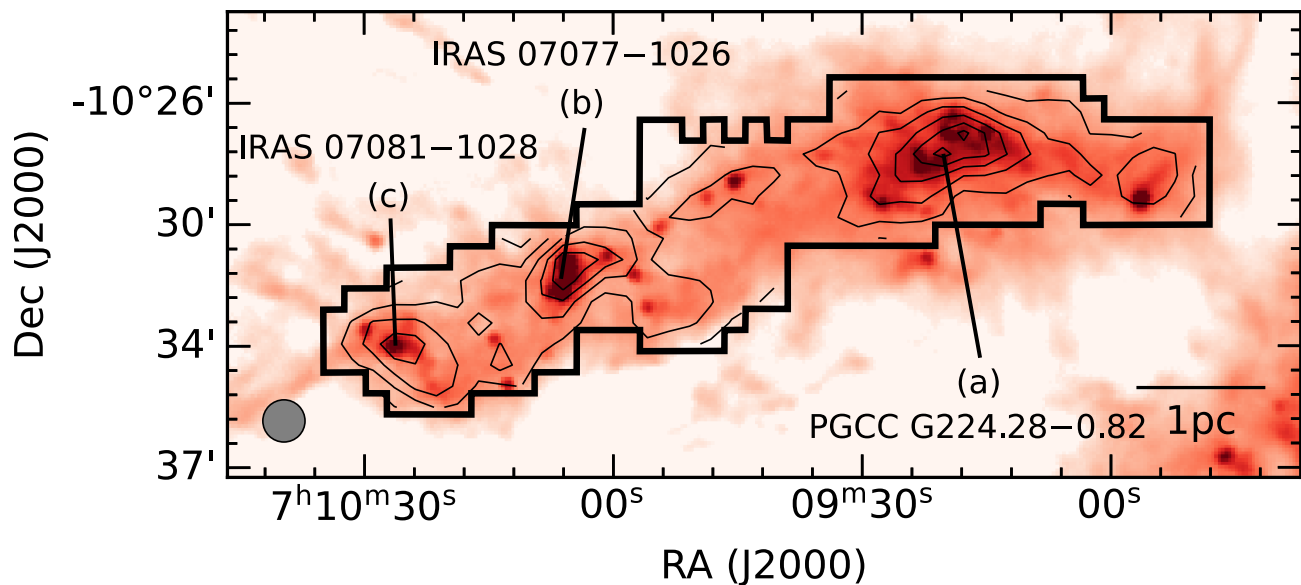


Fig. 1. The NH_3 (1,1) integrated intensity map of KAG71 in contours over the *Herschel*/SPIRE 250 μm dust continuum image. The integrated velocity range is from 11.9 km s^{-1} to 19.0 km s^{-1} , containing only the main quadrupole hyperfine line. The black polygon outlines the mapping area of the NH_3 observations. The labels (a) – (c) indicate the positions for the spectra of figures 2-(a) to (c). The lowest contour and contour steps are 0.2 K km s^{-1} and 0.4 K km s^{-1} , respectively. The Nobeyama 45 m beam size at 23 GHz is indicated by the grey filled circle shown in the lower left corner. (Color online)

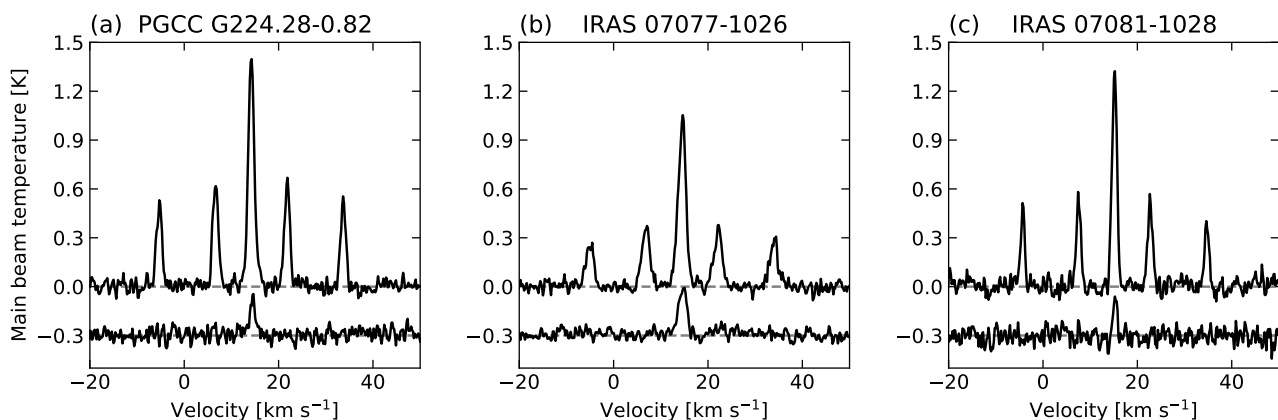


Fig. 2. Panel (a) – (c) : The spectra in the NH_3 (1,1) (top) and (2,2) (bottom) at the position assigned in figure 1 with the same labels. (Color online)

gion associated with the Canis Major (CMA) OB1 region. Figure 1 shows the our observed area superimposed on the *Herschel*¹ (Pilbratt et al. 2010) 250 μm dust continuum image. This star-forming region is one of the targets of KAGONMA (Kagoshima Galactic Object survey with Nobeyama 45-metre telescope by Mapping in Ammonia lines) survey project (Murase et al. 2022; Kohno et al. 2022, 2023), which is identified as KAGONMA 71 (hereafter KAG71). KAG71 corresponds to Canis Major Group 00 (Fischer et al. 2016) and Hi-GAL $l = 224^\circ$ region main filament (Olmí et al. 2016). KAG71 contains Planck Catalogue of Galactic Cold Clumps (PGCC: Planck

Collaboration et al. 2016a) G224.28–0.82, IRAS 07077–1026, and IRAS 07081–1028. Elia et al. (2013) reported that the dust temperature, derived from the *Herschel* dust continuum data, was between 11 K and 13 K in most of this region. They also identified compact objects such as cores and clumps, and reported that most of the compact objects were associated with protostars. Previous studies have reported cluster formations (Fischer et al. 2016; Sewilo et al. 2019) and identified the outflows from protostars associated with clusters (Sewilo et al. 2019; Lin et al. 2021). This suggests that our target is a very young and active star-forming region. The distance to CMA OB1 is estimated by various methods and is still uncertain: 1150 pc based on the colour magnitude diagram (Clariá 1974), $990 \pm 50 \text{ pc}$ based on $uvby\beta$ photometry (Kaltcheva & Hilditch

¹ *Herschel* is an ESA space observatory with science instruments provided by European-led Principal Investigator consortia and with important participation from NASA.

2000), and 1100 pc based on kinematic distances derived from ^{13}CO ($J=1-0$) data (Kim et al. 2004). There are several molecular clouds in the line-of-sight to CMa OB1. Their distances are individually estimated from kinematic distances using CO ($J=1-0$) data (Elia et al. 2013), and a cloud corresponding to KAG71 is at a distance of 900 pc. We adopt 900 pc to be consistent with previous studies (Elia et al. 2013; Sewilo et al. 2019).

This paper is organised as follows: in section 2, we describe the set-up of our observations, data reduction, and archival data sets. In section 3, we present the results of the spatial distribution of the NH_3 emission, the C^{18}O ($J=1-0$) emission and the dust continuum emission. The difference of spatial distributions is discussed and possible causes are described in section 4. In section 5, we summarise our results and conclusions.

2 Observations and data

2.1 NH_3 and H_2O Maser Observations

We made mapping observations covering an area of $26' \times 10'$ area (figure 1) with the Nobeyama 45 m radio telescope² from 2016 December to 2019 May. These observations used a high electron mobility transistor receiver, H22, and an auto-correlation spectrometer, the Spectral Analysis Machine for the 45 m telescope, SAM45 (Kuno et al. 2011). The metastable NH_3 inversion transitions at $(J, K) = (1, 1)$, $(2, 2)$, and $(3, 3)$, and H_2O maser were observed simultaneously in both circular polarisations. We observed 295 positions on a $37''.5$ grid in the equatorial coordinates and the three-ON points position-switch observations. The half-power beam width (HPBW) varies slightly between the observing seasons and between the two circular polarisations (see table 1). We refer to $75''$ (corresponding to 0.33 pc at 900 pc), which is twice the grid size, as the effective beam size of the map instead of the HPBW. The OFF position was taken at $(\alpha_{J2000}, \delta_{J2000}) = (07:09:20.31, -10:27:55.35)$, where no NH_3 emission lines and no H_2O maser emission line were detected. The pointing accuracy was checked every hour using the H_2O maser sources associated with IK Tau, VY CMa, and Z Pup, and was within $7''$. The rest frequencies NH_3 ($J, K) = (1, 1)$, $(2, 2)$, $(3, 3)$, and H_2O maser are 23.694495 GHz, 23.722633 GHz, 23.870129 GHz, and 22.235080 GHz, respectively. The bandwidth and frequency resolution are 62.5 MHz and 15.26 kHz, respectively, corresponding to 400 km s^{-1} and 0.19 km s^{-1} at the NH_3 (1,1) frequency. During the observations, the system noise temperature, T_{sys} , that is the

noise contributions from the atmosphere and the receiver, was between 100 K and 1000 K, or typically 200 K. The antenna temperature (T_a^*) was calibrated by the chopper wheel method. The observations at position (a) in figure 1 were made at the beginning of each observation from December 2018 to March 2019. Twenty-eight observations were made, and the NH_3 (1,1) peak intensity had a variation of about 7% at 1σ . The calibration accuracy of intensity is therefore $\sim 7\%$.

Data reductions were performed using the Java NEWSTAR software package developed at the Nobeyama Radio Observatory (NRO). Baseline correction was performed with a third-order polynomial for emission-free channels. The main beam efficiency (η_{mb}) at 23 GHz is different for each observation season and polarisation (see table 1). We used the mean value, 83.5%, as η_{mb} for the whole observation season to convert from T_a^* to T_{mb} . To check the consistency and reduce the noise level, we observed one or more times at the same position and averaged both polarisation data with a weight of $1/\text{rms}^2$. To reduce the noise level, we also smoothed the NH_3 data to a velocity resolution of 0.38 km s^{-1} . The resulting rms noise level (hereafter σ_{rms}) is typically 0.027 K on the T_{mb} scale. For the H_2O maser observations, a conversion factor of 2.8 Jy K^{-1} was used to convert the antenna temperature to flux density.

2.2 Archival Data / Catalogue

We used the ^{12}CO ($J=1-0$) and C^{18}O ($J=1-0$) data cubes obtained with the Mopra 22 m telescope³ (Olmli et al. 2016). The beam size and velocity resolution are $38''$ and 0.09 km s^{-1} , respectively. We used the main beam efficiency of 0.42 (Ladd et al. 2005) measured at 115 GHz to convert the antenna temperature to the brightness temperature. Baseline correction was performed with a first-order polynomial for emission-free channels. To reduce the noise level, we smoothed over six spectral channels and the resulting velocity resolution is $\simeq 0.55 \text{ km s}^{-1}$. We have also produced regridded data with a grid size of $14''$ for comparison with the *Herschel* dust continuum data. The mean rms noise of the $14''$ data is 0.39 K for ^{12}CO and 0.18 K for C^{18}O on the T_{mb} scale, respectively. Although the observed area of the Mopra data does not cover the whole of our NH_3 observed area, the uncovered area is small; about $2'$ at the eastern and western edges of our area.

In order to understand the C^{18}O distribution in the entire NH_3 observed area, we also used the C^{18}O ($J=1-0$) data cube from FOREST Unbiased Galactic plane imaging

² The Nobeyama 45 m radio telescope is operated by the Nobeyama Radio Observatory, a branch of the National Astronomical Observatory of Japan.

³ <https://cdsarc.cds.unistra.fr/viz-bin/cat/J/A+A/594/A58>

Table 1. The HPBW and main-beam efficiency at each polarisation for each observation season.

season	HPBW (RHCP)	HPBW (LHCP)	η_{mb} (RHCP)	η_{mb} (LHCP)
2015-2016	$74''.4 \pm 0''.3$	$73''.9 \pm 0''.3$	$83\% \pm 4\%$	$84\% \pm 4\%$
2016-2017				
2017-2018	$73'' \pm 1''$	$72'' \pm 1''$	$84\% \pm 2\%$	$83\% \pm 2\%$
2018-2019				

survey (FUGIN⁴: Umemoto et al. 2017), which is one of the legacy projects of the NRO. The FUGIN ¹²CO ($J=1-0$) data cube was also used to check the intensity consistency between the Mopra data and the FUGIN data. The effective beam size and velocity resolution are $20''$ and 1.3 km s^{-1} respectively. The mean rms noise is 3.6 K for ¹²CO and 1.5 K for C¹⁸O on the T_{mb} scale, respectively. We smoothed the C¹⁸O data to become its beam size of $75''$ and regridded it to a grid size of $37''.5$ to match our NH₃ maps using the Astronomical Image Processing System (AIPS) software. The resulting mean rms noise is 0.25 K.

The original FUGIN C¹⁸O data are not sensitive enough, and the Mopra CO isotopologue lines data are smaller than our observed area. This makes it difficult to compare the intensity distributions of the C¹⁸O line and the NH₃ line. In this paper, we used the smoothed FUGIN C¹⁸O data to compare the line intensity distribution between C¹⁸O and NH₃, and the Mopra data for comparison with dust properties. The Mopra ¹²CO intensity is about 30% higher than the FUGIN ¹²CO intensity, the C¹⁸O intensities agree within 5%. We discuss the effects of the different ¹²CO intensities on the physical parameters in appendix 1.

To understand the spatial distribution and physical conditions of the dust, we used the *Herschel* dust continuum data from $160 \mu\text{m}$ to $500 \mu\text{m}$ with the identification numbers (OBSID) 1342220650 and 1342220651. These were obtained from the *Herschel* Science Archive⁵. These data are a part of the *Herschel* Infrared GALactic Plane Survey (Hi-GAL) key project (Molinari et al. 2010). Different detectors were used for each wavelength range: for $160 \mu\text{m}$, the Photodetector Array Camera and Spectrometer (PACS: Poglitsch et al. 2010), and for $250 \mu\text{m}$, $350 \mu\text{m}$, and $500 \mu\text{m}$, the Spectral and Photometric Imaging REceiver (SPIRE: Griffin et al. 2010). We used the Level 2.5 data for each wavelength range. The *Herschel* PACS Level 2.5 calibrated data provide only relative photometry. We need to add a zero-level offset to the $160 \mu\text{m}$ data. The offset calculation was performed by comparing *Herschel* with dust properties data released by the *Planck* collaboration

(Planck Collaboration et al. 2016b), following the method of Lombardi et al. (2014). Because the *Planck* data are at $5'$ resolution, we smoothed the *Herschel* $160 \mu\text{m}$ data to $5'$ resolution for comparison and derived the offset value of $-73.7 \text{ MJy sr}^{-1}$ at $5'$ resolution. We added this value to the original resolution *Herschel* data. The beam of each wavelength is elongated along the scan direction during the observation. However, the elongation is small enough for discussion in this paper. Therefore, we used the geometric mean as the beam size. The beam size of four bands from $160 \mu\text{m}$ to $500 \mu\text{m}$ are $12''.6$, $18''.4$, $25''.2$, and $36''.7$, respectively⁶.

To study the impact of protostars on the interstellar medium, we used the catalogue of protostar candidates reported in Sewilo et al. (2019). We only used YSO candidates for which the physical parameters were derived by spectral energy distribution (SED) fitting.

3 Results

3.1 Data overview

Figure 2 shows the NH₃ (1,1) and (2,2) spectra at the position (a) – (c) of figure 1. In our observations, we can find 5 quadrupole hyperfine lines consisting of one main quadrupole hyperfine line, two inner quadrupole satellite hyperfine lines, and two outer quadrupole satellite hyperfine lines in the (1,1) transition. In the (2,2) transitions only the main quadrupole hyperfine line was detected. Weak emission in the (3,3) main quadrupole hyperfine line ($T_{\text{mb}} \simeq 0.11 \text{ K}$) was detected in the central position of IRAS 07077–1026 (position (b) shown in figure 1).

Figure 3-(a) shows the integrated intensity map of the NH₃ (1,1) main quadrupole hyperfine line. We found three bright regions in the NH₃ emission associated with PGCC G224.28–0.82, IRAS 07077–1026, and IRAS 07081–1028. The spatial distribution of the NH₃ emission is consistent with the *Herschel* dust continuum emission. This suggests that NH₃ emission lines are good tracers of dense molecular gas. The detailed analysis is described in subsection 3.5 and intensity correlations between the NH₃ (1,1) emission and the $250 \mu\text{m}$ dust emission are described in appendix 2.

⁴ <http://jvo.nao.ac.jp/portal/nobeyama/fugin.do>

⁵ <http://archives.esac.esa.int/hsa/whsa/>

⁶ See details in photometer quick-start guide of each instrument. <https://www.cosmos.esa.int/web/herschel/legacy-documentation>

Table 2. Coordinates and flux variations of H₂O masers.

ID	RA	Dec	1st observation	2nd observation	3rd observation
1	07:08:57.4	−10:29:10	6.25 Jy	6.12 Jy	2.05 Jy
			03/12/2018	08/12/2018	16/02/2019
2	07:09:17.7	−10:26:40	1.73 Jy		
			14/02/2016		
3	07:09:55.9	−10:31:03	0.85 Jy	0.76 Jy	
			08/05/2017	05/15/2017	

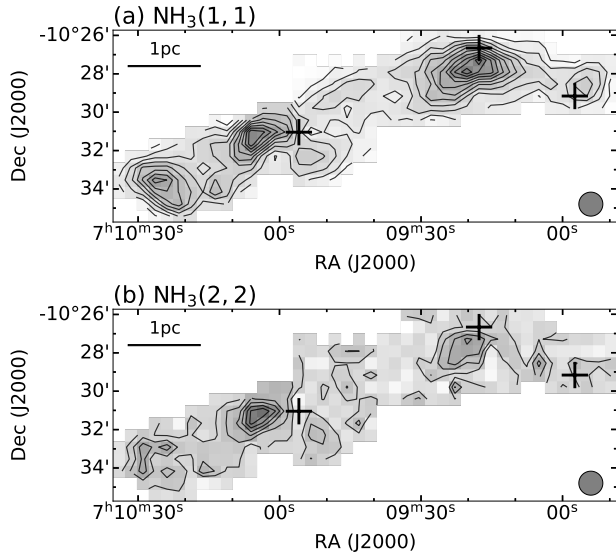


Fig. 3. (a): Integrated intensity map of NH₃ (1,1). The lowest contour and contour steps are 0.2 K km s^{−1} on the T_{mb} scale. Black crosses show the positions of the H₂O maser emission. (b): in (2,2). The lowest contour and contour steps are 0.1 K km s^{−1}. In each panel, the integrated velocity range is from 11.8 km s^{−1} to 19.0 km s^{−1}. The beam size is indicated by the grey filled circle shown in the bottom right corner of each panel. (Color online)

Although the NH₃ beam size (~ 0.3 pc) is larger than the typical filament width (~ 0.1 pc), the spatial distribution of the NH₃ emission is expected to reflect the filamentary structure derived from the dust emission reported by Schisano et al. (2014) and Sewilo et al. (2019).

Figure 3-(b) shows the integrated intensity map of NH₃ (2,2) main quadrupole hyperfine line. The NH₃ (2,2) line was detected in the region where (1,1) was strongly detected, and the strongest emission was detected in IRAS07077–1026. This implies that IRAS 07077–1026 has a higher temperature than the other regions.

We detected three new H₂O maser sources. Table 2 shows the position, flux densities and observation dates of each maser source. Table 2 shows the centres of the highest intensity pixels. While IRAS 07077–1026 was reported to be associated with a H₂O maser (e.g., Brand et al. 1994; Sunada et al. 2007), it was not detected in our observations. Detected maser spectra are shown in figure 16.

3.2 Ammonia line fitting

In case where the velocity dispersion $\gtrsim 0.2$ km s^{−1}, NH₃ (1,1) emission are observed only 5 quadrupole hyperfine lines. These quadrupole hyperfine lines which splitted by electric quadrupole interactions, are further composed 18 magnetic hyperfine lines by magnetic spin-spin interactions. In this paper we refer to magnetic hyperfine lines as hyperfine components (HCs) and to quadrupole hyperfine lines as hyperfine component groups (HCGs). These HCGs are traditionally called the main quadrupole hyperfine line, 2 inner quadrupole satellite hyperfine lines, and 2 outer quadrupole satellite hyperfine lines, which consist of 8, 3, and 2 HCs, respectively (see Ho et al. 1977; Rydbeck et al. 1977; Ho & Townes 1983; Wang et al. 2020, for details).

To obtain the line width, we performed a relative intensity weighted Gaussian fit to all 18 HCs simultaneously at each observed position using the following equation (similar fitting procedure is described in Dhabal et al. 2019):

$$T_{\text{mb}}(v) = \sum_{n=1}^5 a_n \sum_i w_i \exp\left(-\frac{v - v_{\text{los}} - \delta v_i}{2\sigma_v^2}\right), \quad (1)$$

where a_n is the peak intensity of each HCG ($n = 1$ to 5) in the case of well-blended HCGs are observed, v_{los} is the line-of-sight velocity of the main quadrupole hyperfine line, σ_v is the velocity dispersion, δv_i is the velocity offset of each HC from v_{los} , and w_i is the fitting weight of each HC ($i = 1$ to 18 calculated from tables 11 and 15 of Mangum & Shirley 2015). The w_1 to w_5 and w_{14} to w_{18} correspond to the relative hyperfine intensities of the magnetic hyperfine. NH₃ (1,1) main quadrupole hyperfine line contains two electric quadrupole hyperfine states of $\Delta F = 0$. Therefore the w_6 to w_{13} are calculated from the relative intensities of the magnetic hyperfine component and the electric quadrupole hyperfine component; the relative intensities of the magnetic hyperfine component are scaled by the relative intensities of the electric quadrupole hyperfine component and the sum of the w_6 to w_{13} is 1. The w_i and δv are summarised in table 3. When the line width of the HCs is narrow, a_n is not equal to the observed peak intensity of each HCG because individual HCs belonging

Table 3. The parameters of hyperfine components for NH₃ (1,1).

HCG	HC number	F' ₁ → F ₁	Relative Intensity ^a	fitting weight w_i ^b	Velocity offset [km s ⁻¹]
Outer quadrupole satellite hyperfine line 1	1	(1,0)	$\frac{2}{3}$	$\frac{2}{3}$	-19.55
	2	(1,0)	$\frac{1}{3}$	$\frac{1}{3}$	-19.41
Inner quadrupole satellite hyperfine line 1	3	(1,2)	$\frac{3}{5}$	$\frac{3}{5}$	-7.82
	4	(1,2)	$\frac{1}{15}$	$\frac{1}{15}$	-7.37
	5	(1,2)	$\frac{1}{3}$	$\frac{1}{3}$	-7.23
Main quadrupole hyperfine line	6	(2,2)	$\frac{1}{25}$	$\frac{1}{30}$	-0.25
	7	(1,1)	$\frac{5}{9}$	$\frac{5}{54}$	-0.21
	8	(2,2)	$\frac{14}{25}$	$\frac{7}{15}$	-0.13
	9	(1,1)	$\frac{1}{9}$	$\frac{1}{54}$	-0.07
	10	(2,2)	$\frac{9}{25}$	$\frac{3}{10}$	0.19
	11	(2,2)	$\frac{1}{25}$	$\frac{1}{30}$	0.31
	12	(1,1)	$\frac{1}{9}$	$\frac{1}{54}$	0.32
	13	(1,1)	$\frac{2}{9}$	$\frac{1}{27}$	0.46
	Inner quadrupole satellite hyperfine line 2	14	(2,1)	$\frac{1}{15}$	$\frac{1}{15}$
15		(2,1)	$\frac{3}{5}$	$\frac{3}{5}$	7.47
16		(2,1)	$\frac{1}{3}$	$\frac{1}{3}$	7.89
Outer quadrupole satellite hyperfine line 2	17	(0,1)	$\frac{2}{3}$	$\frac{2}{3}$	19.32
	18	(0,1)	$\frac{1}{3}$	$\frac{1}{3}$	19.85

^a The relative intensities are taken from table 15 of Mangum & Shirley (2015). The sum of the relative intensities of each of magnetic hyperfine splittings associating with each quadrupole hyperfine splitting are 1.

^b The intensity ratio of (F'₁, F₁) = (1,1) to (2,2) is five to one; this ratio is used to correct for fitting weights of the main group.

to the same HCG do not overlap sufficiently, and the shape of the HCG does not follow a single Gaussian profile. Since the line width obtained from our observations are broad, we assume that a_n is equal to the observed peak intensity of each HCG. We assume that all 18 HCs have a same velocity dispersion, and each HC at the same HCG does not cause a hyperfine intensity anomaly.

We used a data cube with a velocity resolution smoothed to 0.38 km s⁻¹ to improve the signal-to-noise ratio (S/N) of the quadrupole satellite hyperfine lines. Line fitting was performed at positions where the main quadrupole hyperfine line detected more than $5\sigma_{\text{rms}}$. When $\sigma_v > 1.0$ km s⁻¹, NH₃ main quadrupole hyperfine line and inner quadrupole satellite hyperfine lines begin to overlap (Zhou et al. 2020). We applied σ_v under the condition of $0.2 \text{ km s}^{-1} < \sigma_v < 1.3 \text{ km s}^{-1}$ to account for noise effects in these fits, because no overlapping profile between main and inner quadrupole satellite hyperfine lines is observed.

Figures 4-(a) and (b) show maps of v_{los} and full width at half maximum (FWHM) line widths estimated by NH₃ (1,1) fittings. We can see a velocity gradient from northwest to southeast. The FWHM ranges from 0.6 km s⁻¹ to 3.1 km s⁻¹. The region of IRAS 07077–1026 shows that

the line widths are broad.

In our observations, only the NH₃ (2,2) main quadrupole hyperfine line was detected. Although the main quadrupole hyperfine line consists of 12 HCs, single Gaussian fits were performed on the NH₃ (2,2) main quadrupole hyperfine line because the frequency of the 12 HCs in the main quadrupole hyperfine line is too close to resolve them in our observations. In these fits, the line widths of the NH₃ (1,1) and (2,2) lines were assumed to be the same (see also Urquhart et al. 2011; Murase et al. 2022), and the fits were performed at positions where the NH₃ (2,2) main quadrupole hyperfine line was detected above $3\sigma_{\text{rms}}$. As with NH₃ (1,1), we used a data with a velocity resolution smoothed to 0.38 km s⁻¹.

The estimated NH₃ physical parameters were used in subsection 3.3. For the line-of-sight velocity and velocity dispersion, the estimated covariances from these fits were taken as errors. For the peak intensity of the NH₃ (1,1) and (2,2) quadrupole hyperfine lines, the estimated covariances and the intensity calibration accuracy $\sim 7\%$ were taken as errors.

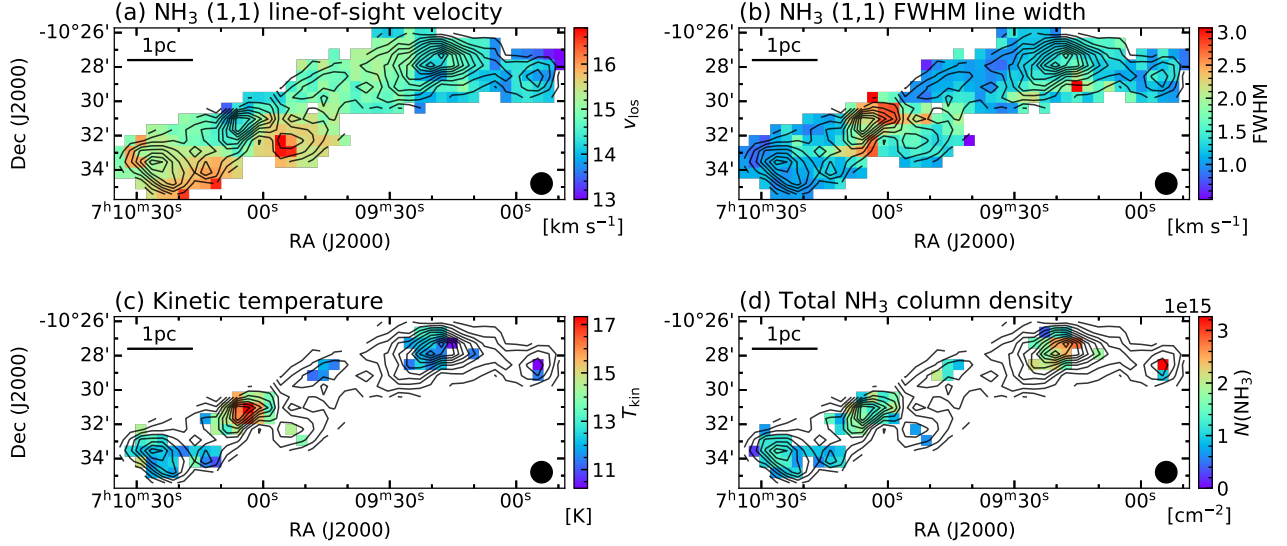


Fig. 4. Spatial distributions of the physical parameters from NH_3 observations. (a): The line-of-sight velocity of the NH_3 (1,1) main quadrupole hyperfine line, (b): FWHM line width from the NH_3 (1,1) lines described in subsection 3.2, (c): Kinetic temperature, and (d): Total NH_3 column density. The contours and the black filled circle in the bottom right corner are the same as in figure 3-(a). (Color online)

3.3 Physical parameters from NH_3 lines

We derived the optical depth, τ , the kinetic temperature, T_{kin} , and the column density, $N(\text{NH}_3)$, from our NH_3 observations.

3.3.1 optical depth τ

Under the local thermal equilibrium (LTE) conditions, the optical depth can be derived from the intensity ratio between the main quadrupole hyperfine line and quadrupole satellite hyperfine lines of the NH_3 (1,1) emission (Ho & Townes 1983). The optical depth can be derived from the following equation:

$$\frac{T_{\text{mb}}(\text{sate})}{T_{\text{mb}}(\text{main})} = \frac{1 - \exp(-a\tau_{(1,1,m)})}{1 - \exp(-\tau_{(1,1,m)})}, \quad (2)$$

where $\tau_{(1,1,m)}$ is the optical depth of the main quadrupole hyperfine line and a is the relative intensity ratio of main quadrupole to quadrupole satellite hyperfine lines, which is 0.27778 for the inner quadrupole satellite hyperfine lines or 0.22222 for the outer quadrupole satellite hyperfine lines (Mangum et al. 1992). In the optically thin case, the a is the ratio of the total intensity of eight HCs forming the main quadrupole hyperfine line to the total intensity of two or three HCs forming the quadrupole satellite hyperfine line (see Mangum & Shirley 2015). When the line width is relatively broad, the HCs are well-blended and each HCG has a single Gaussian profile, so the a is approximately equal to the peak intensity ratio of the main quadrupole hyperfine line to the inner or outer quadrupole satellite hyperfine line. However, when the line width is

narrow, the internal HCs are separated at each HCG and the a does not match the peak intensity ratio between the main quadrupole hyperfine line and the inner or outer quadrupole satellite hyperfine line (see Zhou et al. 2020; Wang et al. 2020). Taking this effect into account, we derived the optical depth from the integrated intensity of the HCGs,

$$\frac{\int T_{\text{mb}}(\text{sate}) dv}{\int T_{\text{mb}}(\text{main}) dv} = \frac{1 - \exp(-a\tau_{(1,1,m)})}{1 - \exp(-\tau_{(1,1,m)})}. \quad (3)$$

To improve the S/N, we used the mean integrated intensity of 2 inner quadrupole satellite hyperfine lines for the quadrupole satellite hyperfine line intensity. The optical depth was calculated for pixels where the peak intensity of both inner quadrupole satellite hyperfine lines is greater than $5\sigma_{\text{rms}}$. The integrated velocity range for each HCG is approximately $v_{\text{los}} \pm 2.6\sigma_v$. In this range, it is possible to integrate 99% of the radiation represented by the Gaussian profile. As a result, the range of $\tau_{(1,1,m)}$ is from 0.3 to 2.2, and the mean value is 0.9.

3.3.2 The gas temperature

We used the following equation to derive the rotational temperature T_{rot} for pixels where the optical depth can be estimated and NH_3 (2,2) main quadrupole hyperfine line was detected above $3\sigma_{\text{rms}}$,

$$T_{\text{rot}}(2,2;1,1) = -41.2 / \ln \left(\frac{-0.282}{\tau_{(1,1,m)}} \right) \times \ln \left[1 - \frac{T_{\text{mb}}(2,2,m)}{T_{\text{mb}}(1,1,m)} \times [1 - \exp(-\tau_{(1,1,m)})] \right]. \quad (4)$$

We converted the rotational temperature to the kinetic temperature using the following equation (Swift et al. 2005):

$$T_{\text{rot}} = T_{\text{kin}} \left\{ 1 + \frac{T_{\text{kin}}}{T_0} \ln[1 + 0.6 \times \exp(-15.7/T_{\text{kin}})] \right\}^{-1}, \quad (5)$$

where T_0 is the energy difference between the (1,1) and (2,2) levels in Kelvin, which is 41.2 K. In the above equation, we used the value of a collision rate between NH_3 and hydrogen molecules reported by Danby et al. (1988).

Figure 4-(c) shows the spatial distribution of T_{kin} . The range of T_{kin} is from 10.2 K to 17.3 K, and the mean value is 12.9 K. We found that the temperature around IRAS 07077–1026 is higher than the other regions.

3.3.3 The column density of NH_3

Under LTE conditions, NH_3 (1,1) column density, $N(1,1)$, can be derived by the following equation (Mangum et al. 1992):

$$N(1,1) = 6.60 \times 10^{14} \frac{T_{\text{rot}}}{\nu(1,1)} \tau_{(1,1,m)} \Delta V_{1/2}, \quad (6)$$

where $\nu(1,1)$ is the rest frequency of NH_3 (1,1) in GHz, and $\Delta V_{1/2}$ is the FWHM of the NH_3 (1,1) main quadrupole hyperfine line in km s^{-1} . The total NH_3 column density, $N(\text{NH}_3)$, is given by the following equation (Mangum et al. 1992):

$$N(\text{NH}_3) = N(1,1) \sum_J \sum_K \left[\frac{2g_J g_I g_K}{3} \exp\left(\frac{23.3 - E(J,K)/k_B}{T_{\text{rot}}}\right) \right], \quad (7)$$

where g_J is the rotational degeneracy, g_I is the nuclear spin degeneracy, and g_K is the K -degeneracy. $E(J,K)/k_B$ is the energy difference (in Kelvin) of each excited state from the ground state, using data from the JPL Molecular Spectroscopy catalogue (Pickett et al. 1998). The total NH_3 column density was calculated up to metastable states of $(J,K) = (6,6)$, assuming that an ortho-to-para ratio is 1. The column density of NH_3 was calculated at positions where the rotational temperature could be derived as described above.

Figure 4-(d) shows that the spatial distribution of $N(\text{NH}_3)$ does not vary significantly in most of the regions. This figure shows that $N(\text{NH}_3)$ is distributed in the range of $2 \times 10^{14} \text{ cm}^{-2}$ to $3.3 \times 10^{15} \text{ cm}^{-2}$, and the mean value is $1.4 \times 10^{15} \text{ cm}^{-2}$.

3.3.4 Error estimation

Estimating the error in observed physical parameters (i.e., optical depth, gas temperature, and column density) is important. In this paper, we evaluated the errors in these

parameters by Monte Carlo method for each pixel (Murase et al. 2022, see for a similar algorithm). There are three following steps in error estimation, and we applied these in turn to equations (3)–(7):

1. consider the known error in the physical parameter as a standard deviation and generate a random number that follows a normal distribution;
2. substitute the best estimate of the known physical parameter + random number into the equation and derive the physical parameter with an unknown error. In the case of estimating the physical parameter using line intensity, multiply the observed value by the random number that follows the flux calibration error;
3. repeat the above 10000 times and derive the standard deviation from the physical parameters obtained and consider it as the error inherent in the physical parameter.

The estimated errors of T_{kin} and $N(\text{NH}_3)$ for NH_3 bright positions are summarised in table 4.

3.4 Physical parameters from CO lines

As a first step to figure out the physical conditions of the gas traced by the C^{18}O emission, we derived the optical depth, τ , the excitation temperature, T_{ex} , and the column density, $N(\text{C}^{18}\text{O})$, derived from the Mopra data. Before estimating these parameters, we performed single Gaussian fits to the C^{18}O line. In this paper, we only used spectra with a $\text{S/N} \geq 3$ to estimate the physical parameters.

Assuming that the ^{12}CO emission is optically thick and the beam-filling factor is unity, the excitation temperature can be estimated by the following equation (e.g., Nagahama et al. 1998):

$$T_{\text{ex}} = 5.53 \left[\ln \left(1 + \frac{5.53}{T_{\text{peak}}(^{12}\text{CO}) + 0.819} \right) \right]^{-1}, \quad (8)$$

where $T_{\text{peak}}(^{12}\text{CO})$ is the peak intensity of the ^{12}CO emission. The T_{ex} ranges from 10.5 K to 17.8 K and the mean value is 13.9 K.

Assuming that the molecular clouds are under the LTE and have the same excitation temperature along the line-of-sight, and the beam-filling factor is unity, the optical depth of C^{18}O can be obtained from the equation (Shimajiri et al. 2014):

$$\tau_{\text{C}^{18}\text{O}} = -\ln \left(1 - \frac{T_{\text{peak}}(\text{C}^{18}\text{O})}{5.27([\exp(5.27/T_{\text{ex}}) - 1]^{-1} - 0.1666)} \right), \quad (9)$$

where $T_{\text{peak}}(\text{C}^{18}\text{O})$ is the peak intensity of the C^{18}O emission. The $\tau_{\text{C}^{18}\text{O}}$ ranges from 0.04 to 0.44 and the mean value is 0.15. The assumption of the beam filling factor=1 underestimates the optical depth, which also affects later

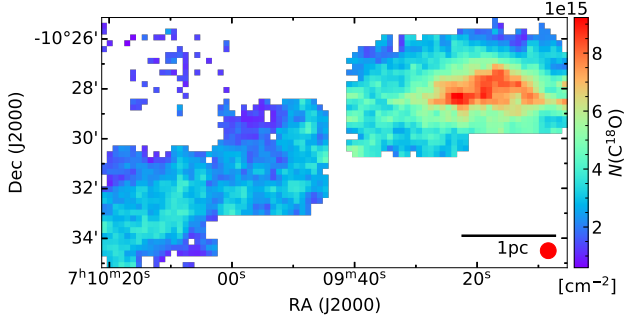


Fig. 5. $C^{18}O$ column density map from the Mopra data. The red filled circle in the bottom right corner indicates the beam size of the Mopra data. (Color online)

estimates of the column density; the extent to which it may underestimate the optical depth is discussed in subsection 4.2.

The column density of $C^{18}O$ can be derived as follows (see Mangum & Shirley 2015, for details):

$$N(C^{18}O) = \frac{3h}{8\pi^3 S \mu^2} \frac{Q_{\text{rot}}}{g_u} \frac{\exp\left(\frac{E}{\kappa_B T_{\text{ex}}}\right)}{\exp\left(\frac{h\nu}{\kappa_B T_{\text{ex}}}\right) - 1} \int \tau dv$$

$$\approx \frac{3h}{8\pi^3 \mu^2} \frac{\exp\left(\frac{5.27}{T_{\text{ex}}}\right)}{\exp\left(\frac{5.27}{T_{\text{ex}}}\right) - 1} \frac{Q_{\text{rot}}}{J_\nu(T_{\text{ex}}) - J_\nu(T_{\text{bg}})} \quad (10)$$

$$\times \frac{\tau_{C^{18}O}}{1 - \exp(-\tau_{C^{18}O})} \int T_{\text{mb}} dv,$$

where $S = J/(2J+1)$ is the line strength, μ is the electric dipole moment, which is 0.11079 Debye for $C^{18}O$, $g_u = 2J+1$ is the level degeneracy, $E/\kappa_B = 5.27$ K is the energy difference of excited state from the ground state in Kelvin, $J_\nu(T) = \frac{h\nu/\kappa_B}{\exp(h\nu/\kappa_B T) - 1}$ is the radiation temperature, and $T_{\text{bg}} = 2.725$ K is the temperature of cosmic microwave background radiation. The rest frequency of the $C^{18}O$ ($J=1-0$) emission line, ν , is 109.782182 GHz. Also, the rotational partition function, Q_{rot} , is given by,

$$Q_{\text{rot}} = \sum_{J=0}^{\infty} (2J+1) \exp\left(-\frac{hB_0 J(J+1)}{k_B T_{\text{ex}}}\right), \quad (11)$$

where B_0 is the rigid rotor rotation constant, which was set to 54891.4 MHz. The electric dipole moment and rigid rotor rotation constant were taken from the JPL molecular spectroscopy catalogue (Pickett et al. 1998). The rotational partition function was calculated up to $J=14$. The errors of all physical parameters are derived by the Monte Carlo method. In these calculations, a flux calibration error of 7% was used as the error for the chopper wheel method (Ulich & Haas 1976).

Figure 5 shows the spatial distribution of the $C^{18}O$ column density. It shows that $C^{18}O$ molecular gases are concentrated at PGCC G224.28–0.82 and that there is no significant feature in the eastern part of the observed area. The $N(C^{18}O)$ ranges from $0.6 \times 10^{15} \text{ cm}^{-2}$ to 9.2×10^{15}

cm^{-2} and the mean value of $N(C^{18}O)$ is $3.4 \times 10^{15} \text{ cm}^{-2}$.

3.5 Deriving dust properties and spatial distributions

Using the *Herschel* dust continuum data, we derived the dust temperature T_{dust} and the molecular hydrogen column density $N(H_2)$, using the wavelengths, λ from 160 μm to 500 μm . We made two data sets, the first is that all wavelength maps were smoothed to the beam size of $36.''7$ and regridded to $14''$, the second is that all wavelength maps were smoothed to the beam size of $75''$ and regridded to $37.''5$. Assuming that a molecular cloud has a single dust temperature along the line-of-sight and that the atomic hydrogen column density is negligibly low, SED fitting towards each pixel was performed by using the following equation:

$$I_\nu = B_\nu(T_{\text{dust}})[1 - e^{-\tau_\nu}], \quad (12)$$

where I_ν is the intensity at frequency ν , $B_\nu(T_{\text{dust}})$ is the Planck blackbody function, $\tau_\nu = \kappa_\nu \Sigma$ is the dust optical depth, κ_ν is the dust opacity per unit mass (dust + gas), $\Sigma = \mu m_H N(H_2)$ is the surface gas density, μ is the mean molecular weight, and m_H is the atomic hydrogen mass. For consistency with Elia et al. (2013), we adopt $\kappa_\nu = \kappa_\lambda = 0.1 \times \left(\frac{\lambda}{250[\mu\text{m}]}\right)^{-\beta} [\text{cm}^{-2} \text{ g}^{-1}]$ assuming a gas-to-dust mass ratio of 100, a dust emissivity index β of 2 (Hildebrand 1983), and $\mu = 2.8$ to take into account a relative helium abundance of 25% by mass (Kauffmann et al. 2008). Following Könyves et al. (2015), each data point of the SED fit was weighted by $1/\sigma_{\text{cal}}^2$, where σ_{cal} is the calibration error of surface brightness (20% at 160 μm and 10% at 250 μm , 350 μm , and 500 μm). Its error estimate uses the covariance matrix.

Figure 6-(a) shows the spatial distribution of the $N(H_2)$. The high-column density is found around PGCC G224.28–0.82, IRAS 07077–1026, and IRAS 07081–1028. The $N(H_2)$ ranges from 0.2×10^{22} to $8.3 \times 10^{22} \text{ cm}^{-2}$.

Figure 6-(b) shows the spatial distribution of the T_{dust} . We can see that the T_{dust} is higher at the edge of the cloud and lower at the centre. This temperature structure has generally been observed in the nearby molecular clouds and infrared dark clouds (e.g., Planck Collaboration et al. 2011; Sokolov et al. 2017). The dust temperature in the NH_3 observed area is 11 K – 14.5 K, which is almost the same as the distribution of the T_{kin} (figure 4-(c)).

Figure 6-(c) shows the map of the NH_3 (1,1) integrated intensity superposed on the $N(H_2)$ derived from the dust continuum emission. In the NH_3 observed area, the NH_3 (1,1) integrated intensity and $N(H_2)$ show good agreement with each other. On the other hand, the region between PGCC G224.28–0.82 and IRAS 07077–1026 has $N(H_2) >$

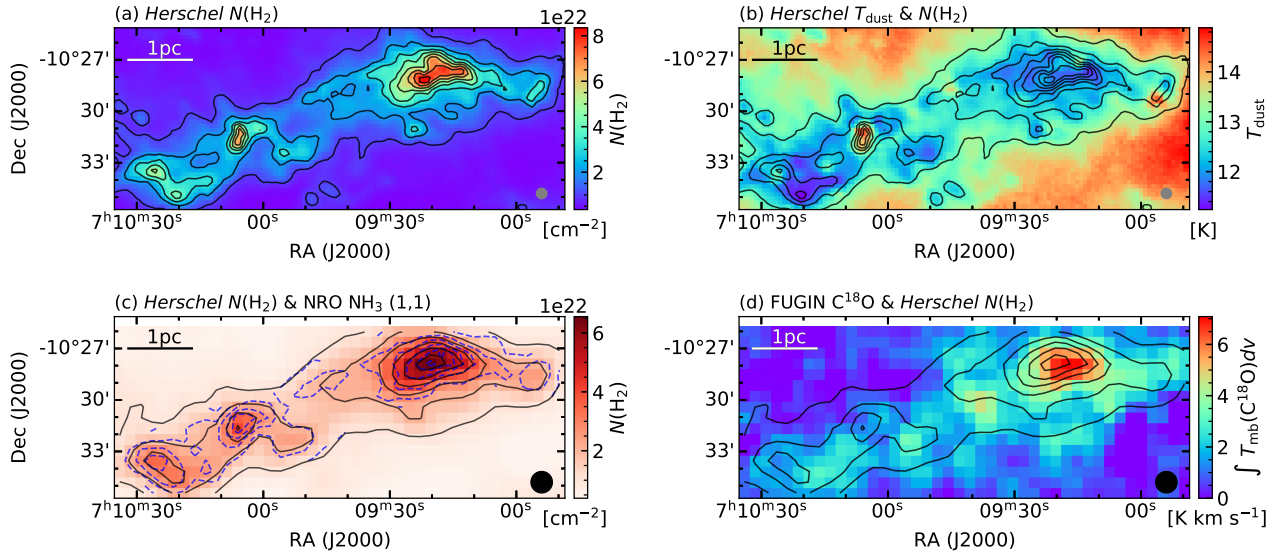


Fig. 6. (a): The colour image and contours indicate the $N(\text{H}_2)$ map obtained in subsection 3.5. The lowest contour and contour steps are $1.0 \times 10^{22} \text{ cm}^{-2}$. (b): The dust temperature image obtained in subsection 3.5. The contours are the same as that shown in panel (a). (c): The colour image and black contours indicate the $N(\text{H}_2)$ map derived from the *Herschel* data smoothed to be the same beam size as the NH_3 data. The lowest contour and contour steps are $1.0 \times 10^{22} \text{ cm}^{-2}$. The blue dashed contours indicate NH_3 (1,1) integrated intensity, which are the same as in figure 1. (d): $N(\text{H}_2)$ distributions (contours) superposed on the C^{18}O integrated intensity map with the velocity range from 11.7 km s^{-1} to 18.9 km s^{-1} (colour image). The black contours are the same as the black contours in panel (c). In all panels, grey filled circle indicates the beam sizes of the *Herschel* data, and black filled circle indicates the $75''$ beam size. (Color online)

$2.0 \times 10^{22} \text{ cm}^{-2}$, while the NH_3 emission is very weak.

Figure 6-(d) shows the $N(\text{H}_2)$ superposed on the map of the FUGIN C^{18}O ($J=1-0$) integrated intensity. We can find no significant correlation between the C^{18}O emission and the spatial distribution of $N(\text{H}_2)$, except for PGCC G224.28–0.82. The C^{18}O emissions were detected in the region between PGCC G224.28–0.82 and IRAS 07077–1026.

3.6 Identification of dense gas clumps with dendrogram

To identify the hierarchical structure of the molecular cloud, we performed a dendrogram analysis (Rosolowsky et al. 2008) on the NH_3 (1,1) main quadrupole hyperfine line data cube, which has a velocity resolution of 0.19 km s^{-1} and a typical rms noise level of 0.035 K . This analysis uses the following three parameters: `min_value`, `min_delta`, and `min_npix`, where `min_value` is a parameter to distinguish between structure and noise, `min_delta` is the threshold to separate multiple structures, and `min_npix` is the minimum number of pixels to identify a structure, respectively. In this paper, we used the input with the `min_value` = 3σ , `min_delta` = 3σ , where $\sigma = 0.035 \text{ K}$ is the rms noise, and `min_npix` = 4 pixels, which is a minimum integer number of pixels larger than the beam size. In addition, we have added the condition that the peak intensity

of the structure is greater than 7σ and that the structure has a spread of two channels or more in the velocity axis. We refer to a "leaf" as a clump in the dendrogram output.

Figure 7 shows the results of the dendrogram analysis. The six NH_3 clumps were identified. We gave an identification number from west to east for each clump. The centre of PGCC G224.28–0.82 corresponds to the clump 2, IRAS 07077–1026 and IRAS 07081–1028 correspond to the clumps 4 and 6, respectively. We adopted $R = \sqrt{A/\pi}$ as the clump radius, where A is the total area on the sky in a clump. The clump radius ranges from 0.19 pc to 0.39 pc . We estimated the mass of each clump using $\text{Mass} = \mu m_{\text{H}} A_{\text{pixel}} \sum_i N_i(\text{H}_2)$, where A_{pixel} is the surface area of the pixel and the $N_i(\text{H}_2)$ is the $N(\text{H}_2)$ of each pixel belonging to each clump. This calculation uses the $N(\text{H}_2)$ data derived in subsection 3.5, which has a resolution of $75''$. The clump mass ranges from $41 M_{\odot}$ to $290 M_{\odot}$. Only the clump 2 is massive enough to fulfil the empirical threshold for high-mass star formation, $M(r) > 870 M_{\odot}$ (radius/pc)^{1.33} (Kauffmann & Pillai 2010). The physical parameters of the clumps are summarised in table 4.

Table 4. Physical properties of the NH₃ clumps identified by the dendrogram.

clump ID	RA	Dec	R [pc]	T_{kin} [K]	FWHM [km s ⁻¹]	$N(\text{NH}_3)$ [cm ⁻²]	Mass [M_{\odot}]
1	07:08:55.9	-10:28:40.5	0.29	10.2 (0.7)	1.32 (0.03)	3.3×10^{15} (6×10^{14})	90 (10)
2	07:09:19.3	-10:27:42.3	0.32	11.6 (0.5)	1.43 (0.01)	2.1×10^{15} (2×10^{14})	290 (30)
3	07:09:51.5	-10:32:17.8	0.23	15 (1)	1.64 (0.05)	7×10^{14} (5×10^{14})	54 (7)
4	07:10:05.4	-10:31:28.2	0.26	16.1 (0.8)	2.18 (0.02)	1.6×10^{15} (3×10^{14})	110 (10)
5	07:10:12.7	-10:33:52.6	0.19	11.5 (0.8)	1.26 (0.02)	1.0×10^{15} (3×10^{14})	41 (6)
6	07:10:24.4	-10:33:47.6	0.39	12.1 (0.7)	1.16 (0.02)	1.4×10^{15} (2×10^{14})	220 (30)

Notes: The physical parameters shown in this table are derived from the positions where the strongest NH₃ (1,1) integrated intensities were obtained for each clump. The errors are shown in parentheses.

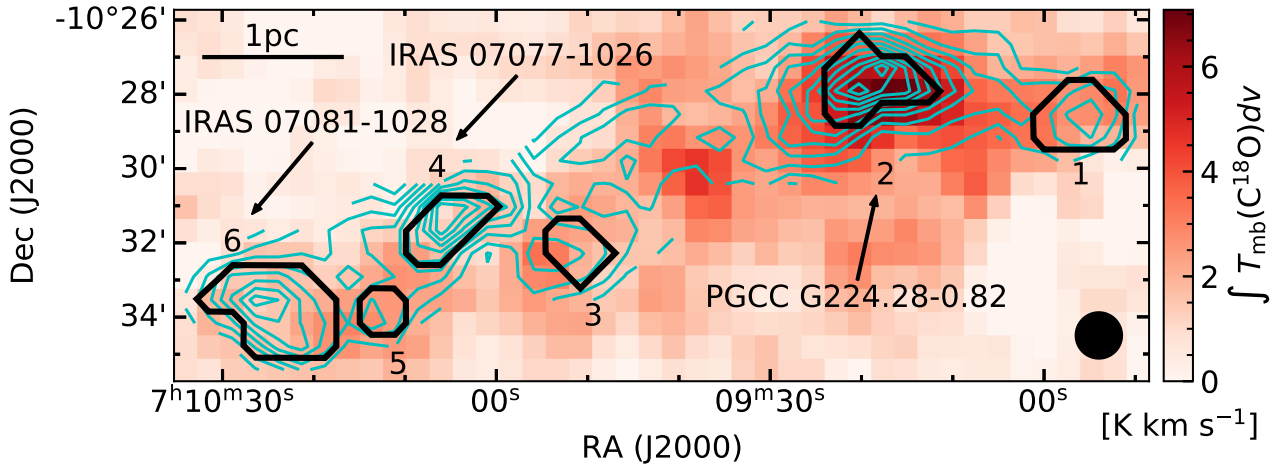


Fig. 7. Integrated intensity map of NH₃ (1,1) in contours over the FUGIN C¹⁸O ($J=1-0$) integrated intensity image. The thick black polygons indicate the position and size of the clumps obtained from the dendrogram analysis in subsection 3.6. The contour steps and the black filled circle in the bottom right corner are the same as figure 3-(a). (Reprinted with permission from Handa et al. (2023). Copyright The Author(s), 2023 Published by Cambridge University Press on behalf of International Astronomical Union.) (Color online)

4 discussion

4.1 Comparison of the NH₃ and C¹⁸O

Figure 7 shows the integrated intensity of the NH₃ (1,1) main quadrupole hyperfine line superposed on the integrated intensity map of the FUGIN C¹⁸O. The spatial distributions of the two emission lines appear to be consistent in most of our observed area, but in particular in the clumps 4 and 6 (IRAS 07077–1026 and IRAS 07081–1028) the distributions are different. The spatial range of the distributional discrepancy is about ~ 1 pc.

If there is a difference for the gas density traced by the NH₃ (1,1) and C¹⁸O ($J=1-0$) emission lines, this could explain the distributional discrepancy. However, we believe these two lines trace almost the same molecular gas because of their line profiles. Figure 8 shows the NH₃ (1,1) and Mopra C¹⁸O ($J=1-0$) spectra. Two panels show the spectra at the clumps 2 and 4, corresponding to positions (a) and (b) in figure 1. For easy comparison, the Mopra C¹⁸O data was smoothed to be the same spatial and velocity resolutions of the NH₃ data. Although the width

of the C¹⁸O is slightly wider than that of the NH₃ (1,1) at either position, the differences are close to the velocity resolution. The two molecular emission lines are likely to trace almost identical layers in the molecular cloud.

To investigate the distributional discrepancy more quantitatively, we made an integrated intensity correlation plot (figure 9). In this plot, we used the pixels contained in the clumps identified by the dendrogram analysis. We can find two features in figure 9: a positive correlation in the clump 2, with a correlation coefficient of $r=0.42$, while negative correlations are found in the clumps 4 and 6, with r of -0.56 and -0.41 , respectively. Since the two lines are expected to trace identical layers in the cloud, our results suggest that the C¹⁸O emission line intensity is suppressed compared to the NH₃ emission in the clumps 4 and 6.

The distributional discrepancy between the integrated intensity of the C¹⁸O ($J=1-0$) and the $N(\text{H}_2)$ or the integrated intensity of the NH₃ (1,1) could have several causes; including CO depletion, photodissociation where the molecules are destroyed by UV radiation, and high-

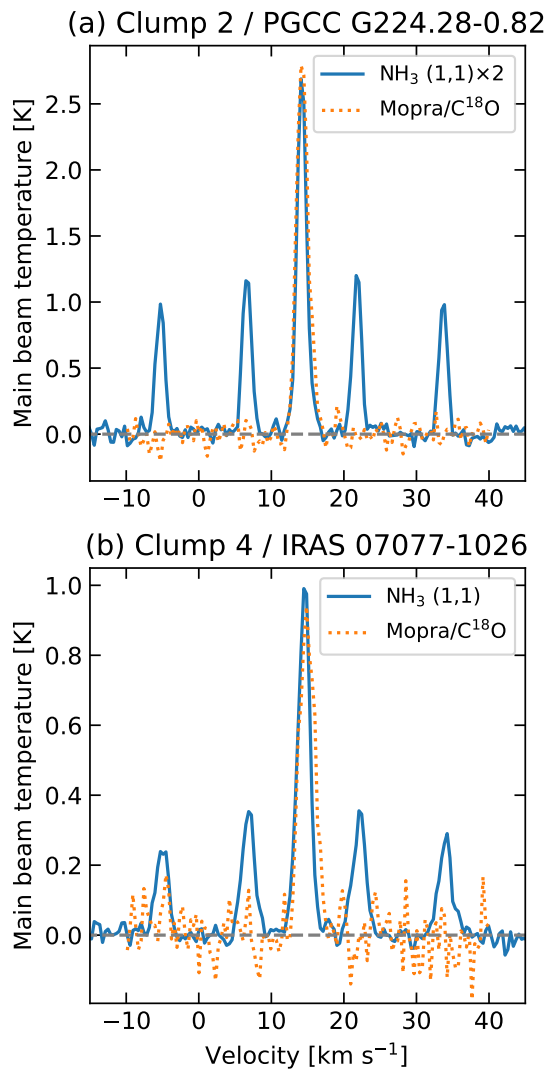


Fig. 8. NH_3 (1,1) and Mopra C^{18}O ($J=1-0$) line profiles of the clumps 2 and 4. The spectra are located at the position (a) and (b) in figure 1. For comparison, both molecular line data were smoothed to the spectral resolution of 0.38 km s^{-1} and Mopra C^{18}O ($J=1-0$) data was smoothed to a beam size of $75''$. (a): Emission line profiles of the clump 2. For easy comparison of line widths, the NH_3 (1,1) intensity is scaled by a factor of 2. (b): Emission line profiles of the clump 4. (Color online)

density gas dissipation. These possibilities will be discussed in subsection 4.3.

4.2 Potential Error of C^{18}O optical depth

The optical depth has a strong influence on the accuracy of column density estimates. In particular, when $\tau > 1$, deriving the reliable column density is difficult because molecular lines cannot trace inside the cloud. Using the brightness temperatures of CO and C^{18}O lines with a $38''$ beam, we derived that the beam averaged optical depths of C^{18}O line are 0.15 - 0.44 and 0.05 - 0.15 for the clumps

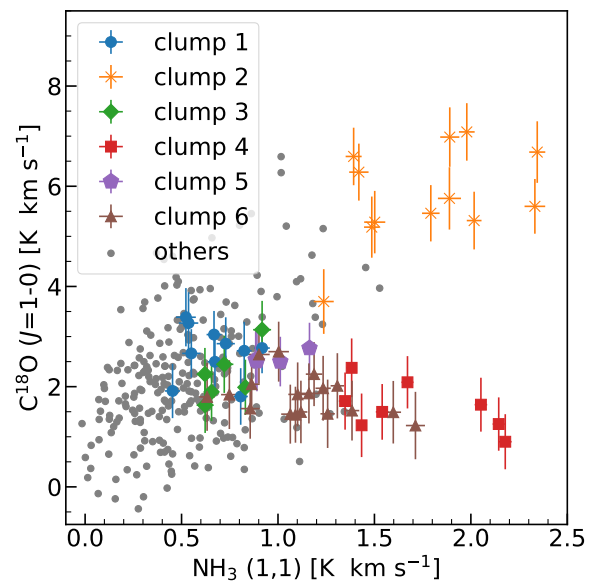


Fig. 9. NH_3 (1,1) - C^{18}O ($J=1-0$) integrated intensity correlation plot of the each clump and the other positions. (Reprinted with permission from Handa et al. (2023). Copyright The Author(s), 2023 Published by Cambridge University Press on behalf of International Astronomical Union.) (Color online)

2 and 4, respectively. It means the estimated column densities are reliable. However, the actual optical depths must be larger in the case of the beam filling factor is less than unity, as a result, the beam averaged column density may be underestimated. It is important to check that the mean optical depth of the emitting region is less than unity.

In the case of NH_3 (1,1) line, the estimated optical depth is free from the beam filling factor, because it is estimated from the intensity ratio of the quadrupole hyperfine lines at the same transition. Therefore, we can estimate the beam filling factor for the NH_3 (1,1) line, ϕ_{NH_3} , assuming that $T_{\text{ex}} = T_{\text{rot}}$. The mean ϕ_{NH_3} over the clump are about 0.15 and 0.09 for the clumps 2 and 4, respectively, for a $75''$ beam. It means the beam filling factor of Mopra C^{18}O ($J=1-0$) is 0.60 and 0.34 for the clumps 2 and 4, respectively, with a $38''$ beam, if the size of C^{18}O ($J=1-0$) emitting area is the same as that of NH_3 (1,1).

Using these values of the beam filling factor, the mean C^{18}O optical depths over the emitting region are 0.30 - 0.90 and 0.14 - 0.50 for the clumps 2 and 4, respectively. In any case, our estimation of the beam averaged column density of C^{18}O is reliable enough.

4.3 Cause of weak C^{18}O emission in dense clump

In subsection 4.1, we showed two regions where the weak C^{18}O emission line is detected despite high H_2 column den-

sity. This phenomenon in the clump 4 was also reported by Olmi et al. (2016). They described two possible causes for this phenomenon: CO depletion and differences in the temperature dependence of CO and dust emissions. It has also been slightly discussed by Sewilo et al. (2019), together with the detection of the H₂O maser, the high density gas has been interpreted as a decrease in the clump 4. However, this phenomenon is hardly discussed in the previous studies and the reason for this discrepancy is not identified. In this subsection we will discuss the cause of this discrepancy, and the clump 4 will be treated as the main subject of discussion unless otherwise stated.

Sewilo et al. (2019) suggested that the gas in the the clump 4 may be decreasing by dissipation. In general, if the gas density is sufficiently lower than the critical density, the molecular emission line cannot be detected. However, N₂H⁺ ($J=1-0$) emission line was detected in this region (Tatematsu et al. 2017). The critical density of N₂H⁺ ($J=1-0$) is $4.1 \times 10^4 \text{ cm}^{-3}$ at $T = 20 \text{ K}$ (Shirley 2015), which is an order of magnitude higher than that of C¹⁸O ($J=1-0$). It is therefore unlikely that the cause of the discrepancy is a decrease in the gas density. Furthermore, the luminosity-mass ratio, L_{bol}/M_{\odot} , of three dust clumps associated with the region within a 1.5 radius of the central position of the clump 4 was less than 1.0 (Elia et al. 2013). Sources with $L_{\text{bol}}/M_{\odot} < 1$ contain either low-mass protostars or early-stage intermediate-mass/high-mass protostars (Molinari et al. 2016). Also, the H₂O maser does not reflect a well-defined evolutionary stage of the host YSOs (Titmarsh et al. 2016). Therefore, the cause of the discrepancy is unlikely to be dense gas dispersion.

We considered that C¹⁸O molecules are likely to be destroyed by photodissociation (e.g., Glassgold et al. 1985). Photodissociation is a phenomenon in which a molecule dissociates when it collides with a high-energy photon. Photodissociation is often detected near the boundary surface between HII regions and molecular clouds. The two IRAS sources reported the candidate for an ultra-compact (UC) HII region (Bronfman et al. 1996). However, two IRAS sources are not listed in the catalogue of the HII region using the Wide-Field Infrared Survey Explorer (Anderson et al. 2014). Furthermore, in and around two IRAS sources, there are no Red MSX Source objects, which are candidates for high-mass young stellar objects and Compact or UC HII regions. Therefore, the clumps 2 and 4 are unlikely to contain a HII region. In addition, the dissociation energies of CO and NH₃ are 11.092 eV and 4.3 eV, respectively (Däppen 2002). It is natural to assume that if a photodissociation region is formed, NH₃ molecules will be destroyed before C¹⁸O molecules, making NH₃ lines undetectable. Furthermore, it is common that for dust

clumps associated with HII region to have $L_{\text{bol}}/M_{\odot} \gtrsim 40$ (Giannetti et al. 2017). Considering that dust clumps associated with the clumps 4 and 6 have $L_{\text{bol}}/M_{\odot} < 2$, the cause of the discrepancy is unlikely to be the destruction of C¹⁸O molecules by photodissociation.

We believe that CO depletion is the most likely cause of the discrepancy. Both the kinetic temperature and the dust temperature in and around the clumps 4 and 6 are lower than 20 K, which is temperature criterion for CO depletion. N₂H⁺ which detected in the clump 4 immediately reacts with CO in the gas-phase to form HCO⁺ (e.g., Jørgensen et al. 2004). In other words, the detection of N₂H⁺ implicitly indicates that CO depletion is occurring at least in the centre of the region. It is therefore suggested that the C¹⁸O line cannot detect high density gas in the clump 4 due to the CO depletion.

Based on this idea, some questions remain as to why CO depletion occurs in the clump 4. First, CO depletion is a temperature dependent phenomenon. It is somewhat unnatural that CO depletion occurs in the clump 4, even though both the dust temperature and the kinetic temperature are higher than the ambient temperature. However, in the clump 4, the dust temperature and the kinetic temperature are 14 K and 17 K, respectively, and CO depletion can occur under these conditions (e.g., Pillai et al. 2007; Fontani et al. 2012; Feng et al. 2020). It is therefore not surprising that CO depletion occurs even at slightly higher temperatures than in the surrounding region. On the other hand, it is also questionable why regions other than clumps 4 and 6 are not affected by CO depletion. In subsection 4.5, a comparison of clump 2 and clump 4 provides a discussion of this question. Second, a SiO emission line is also detected in IRAS 07077–1026 (Harju et al. 1998). This suggests that the outflow shock associated with a protostar destroys the icy mantle of dust grains. However, the outflow shock is highly directional and is unlikely to affect the entire clump. In fact, outflow and CO depletion have been found to occur simultaneously (Tobin et al. 2013; Feng et al. 2016a, 2016b). Therefore, this idea is consistent with previous studies.

It is unclear whether CO depletion occurs everywhere within the clump; Olmi et al. (2023) reported that an ALMA observation of dust clump within the clump 4, named HG2825, has detected strong C¹⁸O ($J=2-1$) emission. Ge et al. (2020) also proposed that there are multiple cores overlapping towards the line-of-sight in this region, forming a complex distribution of different molecular species. High-resolution CO observations over the entire clump are necessary to understand the inner structure.

The clump 6 shows similar features to the clump 4 on the integrated intensity correlation plot of the NH₃ (1,1)

and $C^{18}O$ ($J=1-0$) (figure 9). However, due to the lack of N_2H^+ observations, it is unclear whether CO depletion occurs in the clump 6. Further observations are needed to verify this.

Our results suggest that the presence of pc-scale CO depletion can be detected by comparing the integrated intensity of NH_3 and $C^{18}O$, such as in low-mass star-forming regions (Willacy et al. 1998). Since molecular clouds are concentrated in the Galactic plane and crowded towards the line of sight, it is difficult to compare the distributions of the dust continuum and $C^{18}O$ line emission, and to accurately estimate the properties of depleted regions. Molecular emission lines can be separated using the velocity field information, and the intensities of the emission lines can be easily compared. In addition, the NH_3 line provides many physical parameters, such as gas temperature and column density (see subsection 3.3). Comparing the intensity distributions of NH_3 and $C^{18}O$ lines will allow us to identify many candidates for pc-scale CO depletion in the Galactic plane and to make statistical arguments about the physical conditions of the pc-scale CO depletion.

4.4 $C^{18}O$ depletion factor

It is a common practice to use the depletion factor, f_D (e.g., Caselli et al. 1999), in order to evaluate the degree of CO depletion. The definition of f_D is as follows,

$$f_D = \frac{X^E(C^{18}O)}{X^O(C^{18}O)}, \quad (13)$$

where $X^E(C^{18}O)$ is the "expected" (i.e., canonical) relative abundance of $C^{18}O$ molecules to molecular hydrogen and $X^O(C^{18}O)$ is the observed one. The $C^{18}O$ abundance of the solar neighbourhood or the $C^{18}O$ abundance predicted by the galactocentric distance are frequently used as the $X^E(C^{18}O)$.

The depletion factor obtained from equation (13) varies by a factor of several, depending on assumptions such as dust opacity. When discussing only a single molecular cloud, focusing on changes in the depletion factor within a cloud would reduce the impact of the underlying assumptions. Therefore, we defined the "relative" depletion factor at the same molecular cloud, f_D^R :

$$f_D^R = \frac{X^M(C^{18}O)}{X^O(C^{18}O)}, \quad (14)$$

where $X^M(C^{18}O)$ is the maximum $X^O(C^{18}O)$ in the observed region. We calculated $C^{18}O$ relative abundance, $X(C^{18}O)$, and the $X(C^{18}O)$ in the NH_3 observed area ranges from 4×10^{-8} to 3.7×10^{-7} . To improve reliability, the value of $X^M(C^{18}O)$ is determined from observed pixels that represent more than 10 times the error of $N(C^{18}O)$, and we adopt 2.5×10^{-7} .

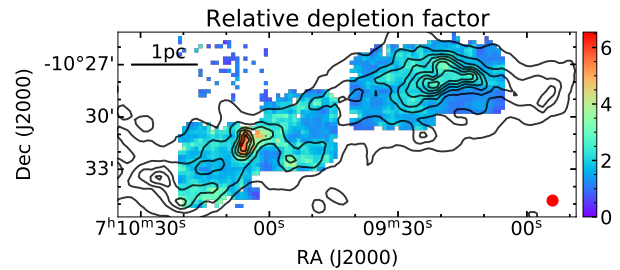


Fig. 10. The spatial distribution of the relative depletion factor, f_D^R . The contours are the same as in figure 6-(a). The red filled circle in the bottom right corner indicates the beam size of the Mopra data. (Color online)

Figure 10 shows the spatial distribution of f_D^R derived from the Mopra data. The f_D^R is about 3.5 to 6.5 in and around the clump 4, and about 1.5 to 3.5 in and around the clump 2. The freeze-out rate of $C^{18}O$ is about 2 to 4 times higher in the clump 4 than in the clump 2.

We found the pc-scale CO depletion in the clump 4 (figure 10). Feng et al. (2020) have reported that $70 \mu m$ dark clumps with pc-scale CO depletion have a depletion factor about 2 to 4 times larger than $70 \mu m$ bright clumps without CO depletion at the same IRDCs. The trend of CO depletion observed in the clump 4 is similar to that of previous studies. While these $70 \mu m$ dark clumps fulfil the empirical threshold for high-mass star formation (Kauffmann & Pillai 2010), the clump 4 is a relatively low-mass clump and is below the empirical threshold. A relatively low-mass clump that cannot form high-mass stars was found to have the same trend of pc-scale CO depletion as high-mass clumps.

4.5 The condition of weak CO depletion in the centre of PGCC G224.28–0.82

From figure 10, we can see that the CO depletion state is different within the observed region. The star-forming clumps located in the observed region can be regarded as having substantially the same external physical conditions and initial conditions for the dense gas formation. It would be important to study the differences in the CO depletion state; the differences in the CO depletion state of the clumps may affect the chemical diversity of the pre/proto-stellar core, since the possibility has been suggested that prestellar cores grow by mass accretion from the surroundings during the protostar formation process (Takemura et al. 2021). In this subsection, we focus on the differences in physical properties between the clump 2 and clump 4.

To investigate the difference in CO depletion state, we compared the temperature and volume density of these clumps. In the clump 2, T_{dust} and T_{kin} are both approximately 12 K, and the mean gas density, calculated assum-

ing the clump is a symmetric sphere, is estimated to be $4 \times 10^4 \text{ cm}^{-3}$. In the clump 4, $T_{\text{dust}} \simeq 14 \text{ K}$, $T_{\text{kin}} \simeq 16 \text{ K}$, and the mean gas density is estimated to be $3 \times 10^4 \text{ cm}^{-3}$.

These estimates fulfil the conditions for the occurrence of CO depletion. In other words, if CO depletion has occurred in the clump 4, it is natural that CO depletion should also occur in the clump 2. The clump 2 fulfils the empirical threshold for high-mass star formation, and intuitively, clump 2 is more likely to cause pc-scale CO depletion than clump 4. Since the gas and dust temperatures at the clump 4 are higher than at the clump 2, and the clumps 2 and 4 also have similar densities, this difference is not caused by temperature and density. In the clump 2, there is only weak CO depletion. Therefore the C^{18}O ($J=1-0$) emission can trace the dense gas. This implies that what determines the conditions under which C^{18}O ($J=1-0$) emission line can and cannot trace dense gas is unclear.

This phenomenon is possibly caused by non-thermal desorption such as photodesorption, chemical sputtering. Molecules frozen onto dust grains may have been released into the gas phase by photodesorption at the clump 2. Figure 11 shows the spatial distribution of f_{D}^{R} and the locations of the protostar candidates reported by Sewilo et al. (2019), classified by bolometric luminosity and evolutionary stages of YSO. As this figure shows, there are three protostars with bolometric luminosity above $100 L_{\odot}$ in the vicinity of only the clump 2. These protostars have only a disk and with no envelope, and can affect the surrounding environment. Furthermore, even protostars deeply embedded in molecular clouds may be able to influence the surrounding environment, if molecular clouds have clumpy structures as proposed by previous studies (e.g., Spaans 1996; Kramer et al. 2008; Shimajiri et al. 2014); as a result, molecules frozen onto dust grains are released into the gas phase by photodesorption.

However, photodesorption is well known to occur in the cold outer regions of proto-planetary disks (e.g., Öberg et al. 2015) as well as in the centre of the pre-stellar core (e.g., Caselli et al. 2012), but it is not known in a cold clump at the pc scale. Therefore, our proposal needs further verification. In order to study the effects of photodesorption by radiation from protostars on the surrounding environment, observations of molecular species such as H_2O , whose abundance increases with photodesorption, are essential.

5 Conclusions

We carried out mapping observations towards the star-forming region, which is the vicinity of $(\alpha_{\text{J2000}}, \delta_{\text{J2000}}) =$

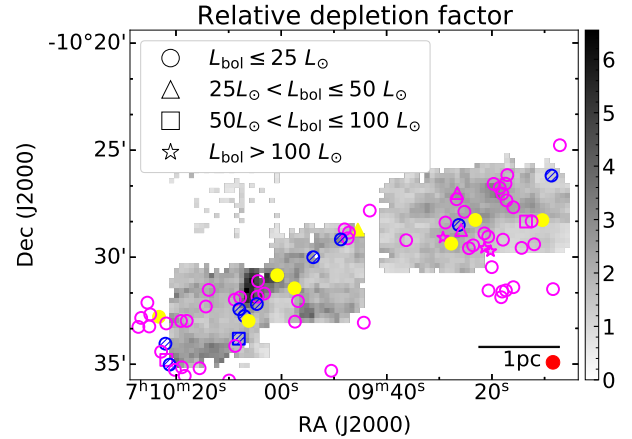


Fig. 11. The locations of the protostar candidates (plots) superposed on the relative depletion factor map (colour image). Magenta open, blue hatched, and yellow filled markers indicate “disk-only” sources, “envelope and disk” sources, and “envelope-only” sources, respectively. The red filled circle in the bottom right corner indicates the beam size of the Mopra data. (Color online)

(07:09:20.30, $-10:27:55$) associated with CMA OB1 in the NH_3 (1,1), (2,2), (3,3), and H_2O maser emission lines using the Nobeyama 45 m radio telescope. Our results are summarised as follows:

1. Our observations revealed physical parameters of the observed region such as T_{kin} and $N(\text{NH}_3)$. The T_{kin} ranges from 10.2 K to 17.3 K, with IRAS 07077–1026 having a higher temperature by about 3 K higher than the other regions. The total column density of NH_3 does not vary significantly in most of the regions. The mean value is $N(\text{NH}_3) = 1.4 \times 10^{15} \text{ cm}^{-2}$.
2. We carried out a dendrogram analysis using NH_3 (1,1) main quadrupole hyperfine line data and identified six clumps. The centre of PGCC G224.28–0.82 corresponds to the clump 2, IRAS 07077–1026 and IRAS 07081–1028 correspond to the clumps 4 and 6, respectively. The clump radius ranges from 0.19 pc to 0.39 pc and clump mass ranges from $41 M_{\odot}$ to $290 M_{\odot}$. Only the clump 2 fulfils the empirical threshold for high-mass star formation.
3. By comparing the spatial distributions of the NH_3 (1,1) integrated intensity and the C^{18}O ($J=1-0$) integrated intensity, we found pc-scale intensity anti-correlations in the clump 4 and clump 6. Moreover, the comparison of these integrated intensity distributions with the distribution of $N(\text{H}_2)$ obtained from the dust shows that the NH_3 molecular emission lines reflect the distribution of $N(\text{H}_2)$ well, even at the pc scale. On the contrary, the intensity distribution of the C^{18}O emission lines does not correlate well with the distribution of $N(\text{H}_2)$, and some high-density regions cannot be de-

tected at the pc scale. By examining the dissipation of the high-density gas, photodissociation, and CO depletion, we suggest that the reason why $C^{18}O$ ($J=1-0$) does not trace $N(H_2)$ is due to CO depletion in the clump 4. A comparison of the intensity distributions of the NH_3 and $C^{18}O$ lines will allow us to identify candidates for pc-scale CO depletion.

4. We calculated the relative depletion factor, f_D^R , and compared the f_D^R of high H_2 column density regions, the clump 2 and clump 4. There are differences in f_D^R by a factor of about 2 to 4. This is comparable to the difference in depletion factor between the 70 μm dark clump and the 70 μm bright clump in the same molecular cloud reported by Feng et al. (2020).
5. We discussed why there is weak CO depletion in the clump 2. The difference in temperature and gas density does not explain this phenomenon well and the conditional differences that $C^{18}O$ ($J=1-0$) can and cannot trace dense gas are unclear. Non-thermal desorption such as photodesorption may play a key role in changing the CO depletion state.

Acknowledgments

The 45 m radio telescope is operated by the Nobeyama Radio Observatory, a branch of the National Astronomical Observatory of Japan. This publication makes use of data from FUGIN, FOREST Unbiased Galactic plane Imaging survey with the Nobeyama 45 m telescope, a legacy project in the Nobeyama 45 m radio telescope. Figure 7 and Figure 9 are reprinted with permission from Handa et al., Parsec scale CO depletion in KAGONMA 71, or a star-forming filament in CMA OB1, Proceedings of the International Astronomical Union, 17(S373), 31-34, 2023. (Copyright The Author(s), 2023 Published by Cambridge University Press on behalf of International Astronomical Union.) This research made use of APLPY, an open-source plotting package for Python (Robitaille & Bressert 2012), ASTROPY,⁷ a community-developed core Python package for Astronomy (Astropy Collaboration et al. 2013, 2018), MATPLOTLIB, a Python package for visualization (Hunter 2007), NUMPY, a Python package for scientific computing (Harris et al. 2020), PANDAS a Python package for statistical analysis, data manipulations and processing (Wes McKinney 2010), SCIPY, a Python package for fundamental algorithms for scientific computing (Virtanen et al. 2020), and Overleaf, a collaborative tool. We would like to thank the Nobeyama Radio Observatory staff members (NRO) for their assistance and observation support. We also thank the students of Kagoshima University for their support in the observations.

⁷<http://www.astropy.org>

Appendix 1 Intensity differences of ^{12}CO

Figure 12 shows the intensity correlation between the Mopra ^{12}CO and the FUGIN ^{12}CO . The FUGIN ^{12}CO data was smoothed to the beam size of the Mopra data and regridded to the grid size of the Mopra data. The Mopra ^{12}CO data was smoothed to the velocity resolution of the FUGIN data and was interpolated onto the FUGIN data grid. The resulting rms noise of the FUGIN ^{12}CO is 1.2 K and that of the Mopra ^{12}CO is 0.30 K. We plot the data for 11 channels ranging from 11.7 $km\ s^{-1}$ to 18.2 $km\ s^{-1}$. They fit well with a linear function of $T_{mb}(FUGIN\ ^{12}CO) = 0.764 \times T_{mb}(Mopra\ ^{12}CO) + 0.127$; the red line overlaid on the data shows the best-fit linear function. The intensity of the Mopra ^{12}CO data is systematically 1/0.764 $\simeq 1.3$ times greater than the intensity of the FUGIN ^{12}CO data. We obtained the result $T_{mb}(FUGIN\ C^{18}O) = 0.973 \times T_{mb}(Mopra\ C^{18}O) - 0.038$ from the similar analysis using the $C^{18}O$ data. There is no significant difference in intensity between the FUGIN $C^{18}O$ and the Mopra $C^{18}O$. It is not known whether the problem is in the FUGIN ^{12}CO data or the Mopra ^{12}CO data and what the cause might be. The following paragraph describes the effect on the physical parameters, in the case of the intensity of the Mopra ^{12}CO data was 30% higher than in reality.

We re-calculated T_{ex} , $\tau_{C^{18}O}$, $N(C^{18}O)$, $X(C^{18}O)$, and f_D^R . The intensity of the Mopra ^{12}CO was scaled by a factor of 0.764 and the following physical parameters were derived without changing other conditions. The T_{ex} changes by a factor of 0.81 to 0.84. The $\tau_{C^{18}O}$ changes by a factor of 1.3 to 1.4. The $N(C^{18}O)$ and the $X(C^{18}O)$ change by a factor of 0.91 to 1.0. The f_D^R changes by a factor of 0.94 to 1.0. Figure 13 shows the re-calculated $N(C^{18}O)$ and figure 14 shows the re-calculated f_D^R . Both the values and the spatial distributions are not significantly different from those before the re-calculation.

Appendix 2 Correlations between NH_3 (1,1) and Dust emission

Figure 15 is the correlation plot between the NH_3 (1,1) integrated intensity and the dust emission intensity at 250 μm . The correlation coefficient between these two data across all pixels is 0.83. There is a clear positive correlation and the same trend regardless of the strength of the two emissions.

Appendix 3 H_2O maser spectrum

Figure 16 shows the spectra of the H_2O masers listed in table 2.

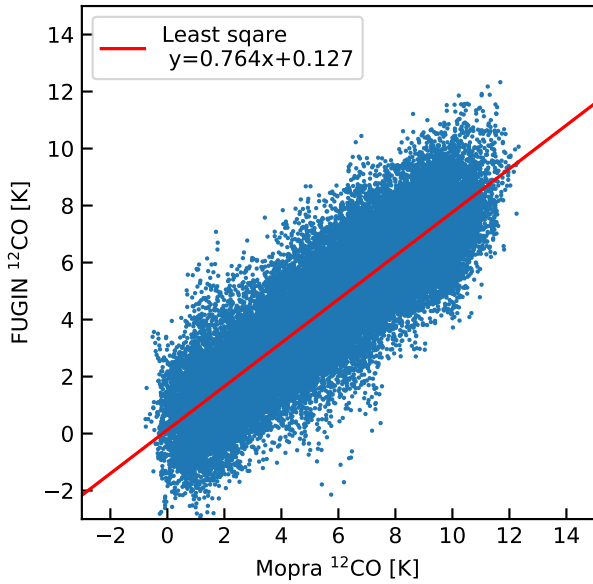


Fig. 12. Intensity correlation between the Mopra ^{12}CO and the FUGIN ^{12}CO . The data from the 11 channels in the range from 11.7 km s^{-1} to 18.2 km s^{-1} are plotted. The red line shows the best-fit linear function determined by a least-squares method. (Color online)

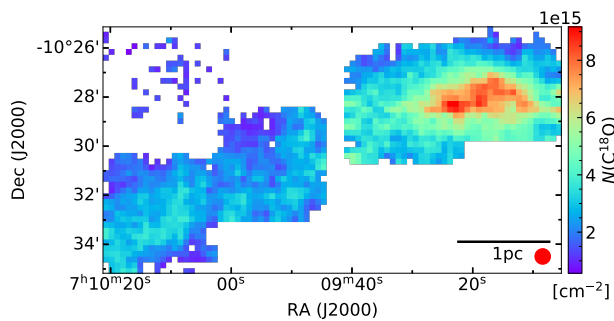


Fig. 13. Same as figure 5 but for the re-calculated C^{18}O column density map derived from the Mopra ^{12}CO data with the intensity scaled by a factor of 0.764. (Color online)

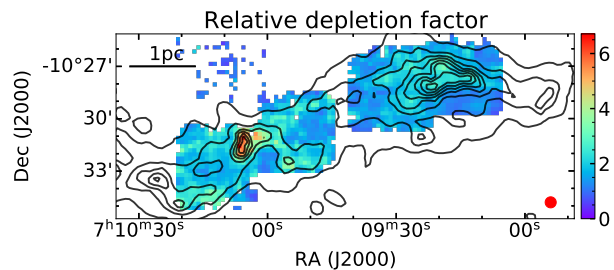


Fig. 14. Same as figure 10 but for the re-calculated relative depletion factor derived from the re-calculated C^{18}O column density. (Color online)

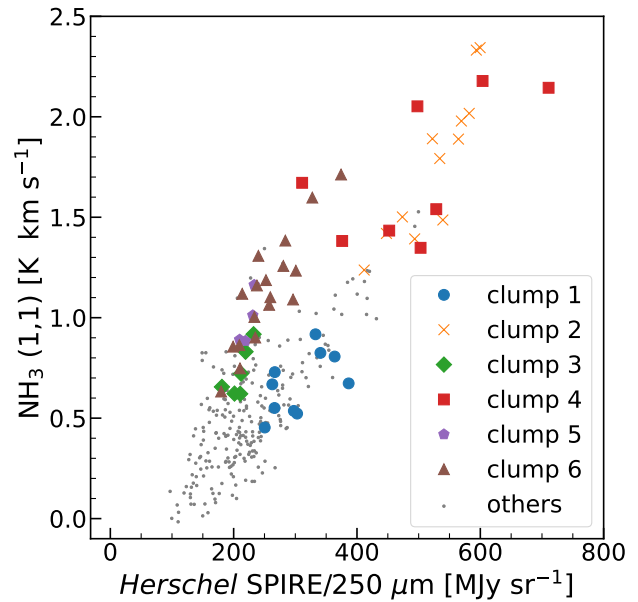


Fig. 15. The correlation diagram between the NH_3 integrated intensity and the dust emission intensity at $250 \mu\text{m}$. The dust emission data was smoothed to a beam size of $75''$. All points are colour coded for each clump and non-clump. (Color online)

Appendix. References

- Anderson, L. D., Bania, T. M., Bailer, D. S., Cunningham, V., Wenger, T. V., Johnstone, B. M., & Armentrout, W. P. 2014, *ApJS*, 212, 1
- Astropy Collaboration, et al. 2013, *A&A*, 558, A33
- Astropy Collaboration, et al. 2018, *AJ*, 156, 123
- Bergin, E. A., & Tafalla, M. 2007, *ARA&A*, 45, 339
- Brand, J., et al. 1994, *A&AS*, 103, 541
- Bronfman, L., Nyman, L. A., & May, J. 1996, *A&AS*, 115, 81
- Caselli, P., Walmsley, C. M., Tafalla, M., Dore, L., & Myers, P. C. 1999, *ApJL*, 523, L165
- Caselli, P., et al. 2012, *ApJL*, 759, L37
- Clariá, J. J. 1974, *A&A*, 37, 229
- Crapsi, A., Caselli, P., Walmsley, M. C., & Tafalla, M. 2007, *A&A*, 470, 221
- Dame, T. M., Hartmann, D., & Thaddeus, P. 2001, *ApJ*, 547, 792
- Danby, G., Flower, D. R., Valiron, P., Schilke, P., & Walmsley, C. M. 1988, *MNRAS*, 235
- Däppen, W. 2002, in *Allen's Astrophysical Quantities*, ed. A. N. Cox (New York: Springer), 27–51
- Dhabal, A., Mundy, L. G., Chen, C.-y., Teuben, P., & Storm, S. 2019, *ApJ*, 876, 108
- Elia, D., et al. 2013, *ApJ*, 772, 45
- Feng, S., Beuther, H., Zhang, Q., Henning, T., Linz, H., Ragan, S., & Smith, R. 2016a, *A&A*, 592, A21
- Feng, S., Beuther, H., Zhang, Q., Liu, H. B., Zhang, Z., Wang, K., & Qiu, K. 2016b, *ApJ*, 828, 100
- Feng, S., et al. 2020, *ApJ*, 901, 145
- Fischer, W. J., Padgett, D. L., Stapelfeldt, K. L., & Sewilo, M. 2016, *ApJ*, 827, 96
- Fontani, F., Giannetti, A., Beltrán, M. T., Dodson, R., Rioja,

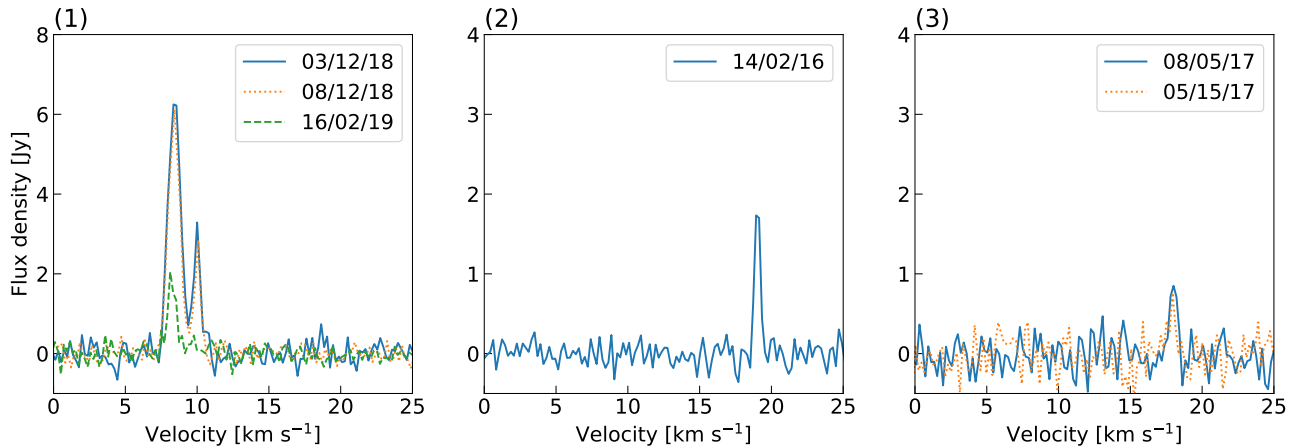


Fig. 16. The H_2O maser emission from our observations. The detected dates and positions are listed in table 2. (Color online)

- M., Brand, J., Caselli, P., & Cesaroni, R. 2012, *MNRAS*, 423, 2342
- Frerking, M. A., Langer, W. D., & Wilson, R. W. 1982, *ApJ*, 262, 590
- Ge, J. X., et al. 2020, *ApJ*, 891, 36
- Giannetti, A., Leurini, S., Wyrowski, F., Urquhart, J., Csengeri, T., Menten, K. M., König, C., & Güsten, R. 2017, *A&A*, 603, A33
- Glassgold, A. E., Huggins, P. J., & Langer, W. D. 1985, *ApJ*, 290, 615
- Gong, Y., Li, G. X., Mao, R. Q., Henkel, C., Menten, K. M., Fang, M., Wang, M., & Sun, J. X. 2018, *A&A*, 620, A62
- Griffin, M. J., et al. 2010, *A&A*, 518, L3
- Handa, T., et al. 2023, *IAU Symposium*, 373, 31
- Harju, J., Lehtinen, K., Booth, R. S., & Zinchenko, I. 1998, *A&AS*, 132, 211
- Harris, C. R., et al. 2020, *Nature*, 585, 357
- Hernandez, A. K., Tan, J. C., Caselli, P., Butler, M. J., Jiménez-Serra, I., Fontani, F., & Barnes, P. 2011, *ApJ*, 738, 11
- Hildebrand, R. H. 1983, *QJRAS*, 24, 267
- Ho, P. T. P., Martin, R. N., Myers, P. C., & Barrett, A. H. 1977, *ApJL*, 215, L29
- Ho, P. T. P., & Townes, C. H. 1983, *ARA&A*, 21, 239
- Hunter, J. D. 2007, *Computing in Science & Engineering*, 9, 90
- Jiménez-Serra, I., Caselli, P., Fontani, F., Tan, J. C., Henshaw, J. D., Kainulainen, J., & Hernandez, A. K. 2014, *MNRAS*, 439, 1996
- Jørgensen, J. K., Schöier, F. L., & van Dishoeck, E. F. 2004, *A&A*, 416, 603
- Kaltcheva, N. T., & Hilditch, R. W. 2000, *MNRAS*, 312, 753
- Kauffmann, J., Bertoldi, F., Bourke, T. L., Evans, N. J., I., & Lee, C. W. 2008, *A&A*, 487, 993
- Kauffmann, J., & Pillai, T. 2010, *ApJL*, 723, L7
- Kim, B. G., Kawamura, A., & Fukui, Y. 2004, *PASJ*, 56, 313
- Kohn, M., et al. 2022, *PASJ*, 74, 545
- Kohn, M., et al. 2023, *PASJ*, 75, 397
- Könyves, V., et al. 2015, *A&A*, 584, A91
- Kramer, C., Alves, J., Lada, C. J., Lada, E. A., Sievers, A., Ungerechts, H., & Walmsley, C. M. 1999, *A&A*, 342, 257
- Kramer, C., et al. 2008, *A&A*, 477, 547
- Kuno, N., et al. 2011, in 2011 XXXth URSI General Assembly and Scientific Symposium, 1–4
- Ladd, N., Purcell, C., Wong, T., & Robertson, S. 2005, *Publ. Astron. Soc. Aust.*, 22, 62
- Lewis, J. A., Lada, C. J., Bieging, J., Kazarians, A., Alves, J., & Lombardi, M. 2021, *ApJ*, 908, 76
- Lin, Z., Sun, Y., Xu, Y., Yang, J., & Li, Y. 2021, *ApJS*, 252, 20
- Lombardi, M., Bouy, H., Alves, J., & Lada, C. J. 2014, *A&A*, 566, A45
- Mangum, J. G., & Shirley, Y. L. 2015, *PASP*, 127, 266
- Mangum, J. G., Wootten, A., & Mundy, L. G. 1992, *ApJ*, 388, 467
- Molinari, S., Merello, M., Elia, D., Cesaroni, R., Testi, L., & Robitaille, T. 2016, *ApJL*, 826, L8
- Molinari, S., et al. 2010, *A&A*, 518, L100
- Murase, T., Handa, T., Hirata, Y., Omodaka, T., Nakano, M., Sunada, K., Shimajiri, Y., & Nishi, J. 2022, *MNRAS*, 510, 1106
- Myers, P. C., & Benson, P. J. 1983, *ApJ*, 266, 309
- Nagahama, T., Mizuno, A., Ogawa, H., & Fukui, Y. 1998, *AJ*, 116, 336
- Öberg, K. I., Furuya, K., Loomis, R., Aikawa, Y., Andrews, S. M., Qi, C., van Dishoeck, E. F., & Wilner, D. J. 2015, *ApJ*, 810, 112
- Olmi, L., Brand, J., & Elia, D. 2023, *MNRAS*, 518, 1917
- Olmi, L., Cunningham, M., Elia, D., & Jones, P. 2016, *A&A*, 594, A58
- Pety, J., et al. 2017, *A&A*, 599, A98
- Pickett, H. M., Poynter, R. L., Cohen, E. A., Delitsky, M. L., Pearson, J. C., & Müller, H. S. P. 1998, *J. Quant. Spectrosc. Radiat. Transfer*, 60, 883
- Pilbratt, G. L., et al. 2010, *A&A*, 518, L1
- Pillai, T., Wyrowski, F., Hatchell, J., Gibb, A. G., & Thompson, M. A. 2007, *A&A*, 467, 207

- Pineda, J. E., Caselli, P., & Goodman, A. A. 2008, *ApJ*, 679, 481
- Planck Collaboration, et al. 2011, *A&A*, 536, A25
- Planck Collaboration, et al. 2016a, *A&A*, 594, A28
- Planck Collaboration, et al. 2016b, *A&A*, 596, A109
- Poglitsch, A., et al. 2010, *A&A*, 518, L2
- Ripple, F., Heyer, M. H., Gutermuth, R., Snell, R. L., & Brunt, C. M. 2013, *MNRAS*, 431, 1296
- Robitaille, T., & Bressert, E. 2012, *APLpy: Astronomical Plotting Library in Python*, ascl:1208.017
- Roccatagliata, V., et al. 2015, *A&A*, 584, A119
- Rosolowsky, E. W., Pineda, J. E., Kauffmann, J., & Goodman, A. A. 2008, *ApJ*, 679, 1338
- Rydbeck, O. E. H., Sume, A., Hjalmarson, A., Ellder, J., Ronnang, B. O., & Kollberg, E. 1977, *ApJL*, 215, L35
- Sabatini, G., Giannetti, A., Bovino, S., Brand, J., Leurini, S., Schisano, E., Pillai, T., & Menten, K. M. 2019, *MNRAS*, 490, 4489
- Sabatini, G., et al. 2022, *ApJ*, 936, 80,
- Schisano, E., et al. 2014, *ApJ*, 791, 27
- Sewilo, M., et al. 2019, *ApJS*, 240, 26
- Shimajiri, Y., et al. 2014, *A&A*, 564, A68
- Shirley, Y. L. 2015, *PASP*, 127, 299
- Sipilä, O., Caselli, P., Redaelli, E., Juvela, M., & Bizzocchi, L. 2019, *MNRAS*, 487, 1269
- Sokolov, V., et al. 2017, *A&A*, 606, A133
- Spaans, M. 1996, *A&A*, 307, 271
- Sunada, K., Nakazato, T., Ikeda, N., Hongo, S., Kitamura, Y., & Yang, J. 2007, *PASJ*, 59, 1185
- Swift, J. J., Welch, W. J., & Di Francesco, J. 2005, *ApJ*, 620, 823
- Tafalla, M., Myers, P. C., Caselli, P., Walmsley, C. M., & Comito, C. 2002, *ApJ*, 569, 815
- Takemura, H., et al. 2021, *ApJL*, 910, L6
- Tatematsu, K., et al. 2017, *ApJS*, 228, 12
- Titmarsh, A. M., Ellingsen, S. P., Breen, S. L., Caswell, J. L., & Voronkov, M. A. 2016, *MNRAS*, 459, 157
- Tobin, J. J., et al. 2013, *ApJ*, 765, 18
- Togi, A., & Smith, J. D. T. 2016, *ApJ*, 830, 18
- Ulich, B. L., & Haas, R. W. 1976, *ApJS*, 30, 247
- Umemoto, T., et al. 2017, *PASJ*, 69, 78
- Urquhart, J. S., et al. 2011, *MNRAS*, 418, 1689
- Virtanen, P., et al. 2020, *Nature Methods*, 17, 261
- Wang, C., Yang, J., Su, Y., Du, F., Ma, Y., & Zhang, S. 2019, *ApJS*, 243, 25
- Wang, S., Ren, Z., Li, D., Kauffmann, J., Zhang, Q., & Shi, H. 2020, *MNRAS*, 499, 4432
- Wes McKinney. 2010, in *Proceedings of the 9th Python in Science Conference*, ed. Stéfan van der Walt & Jarrod Millman, 56 – 61
- Willacy, K., Langer, W. D., & Velusamy, T. 1998, *ApJL*, 507, L171
- Zhou, D.-d., Wu, G., Esimbek, J., Henkel, C., Zhou, J.-j., Li, D.-l., Ji, W.-g., & Zheng, X.-w. 2020, *A&A*, 640, A114